The Astrophysical Journal, 900:164 (23pp), 2020 September 10 https://doi.org/10.3847/1538-4357/abacbe

Is Extended Hard X-Ray Emission Ubiquitous in Compton-thick AGN?

Jingzhe Ma[1], Martin Elvis[1], G. Fabbiano[1], Mislav Baloković[1,2], W. Peter Maksym[1], Mackenzie L. Jones[1], and Guido Risaliti[3]
[1] Center for Astrophysics, Harvard & Smithsonian, 60 Garden Street, Cambridge, MA 02138, USA; jingzhe.ma@cfa.harvard.edu
[2] Black Hole Initiative at Harvard University, 20 Garden Street, Cambridge, MA 02138, USA
[3] INAF- Osservatorio Astrofisico di Arcetri, Largo E. Fermi 5 I-50125 Firenze, Italy
Received 2020 June 2; revised 2020 August 3; accepted 2020 August 4; published 2020 September 14

Abstract

The recent Chandra discovery of extended ∼kiloparsec-scale hard (>3 keV) X-ray emission in nearby Compton-thick (CT) active galactic nuclei (AGN) opens a new window to improving AGN torus modeling and investigating how the central supermassive black hole interacts with and impacts the host galaxy. Since there are only a handful of detections so far, we need to establish a statistical sample to determine the ubiquity of the extended hard X-ray emission in CT AGN and quantify the amount and extent of this component. In this paper, we present the spatial analysis results of a pilot Chandra imaging survey of seven nearby ($0.006 < z < 0.013$) CT AGN selected from the Swift-BAT spectroscopic AGN survey. We find that five out of the seven CT AGN show extended emission in the 3–7 keV band detected at $>3\sigma$ above the Chandra point-spread function (PSF), with ∼12%–22% of the total emission in the extended components. ESO 137-G034 and NGC 3281 display biconical ionization structures with extended hard X-ray emission reaching kiloparsec scales (∼1.9 and 3.5 kpc in diameter). The other three show extended hard X-ray emission above the PSF out to at least ∼360 pc in radius. We find a trend that a minimum 3–7 keV count rate of 0.01 counts s^{-1} and total excess fraction >20% are required to detect a prominent extended hard X-ray component. Given that this extended hard X-ray component appears to be relatively common in this uniformly selected CT AGN sample, we further discuss the implications for torus modeling and AGN feedback.

Unified Astronomy Thesaurus concepts: Active galaxies (17); X-ray active galactic nuclei (2035); AGN host galaxies (2017)

1. Introduction

The recent Chandra discovery of hard (>3 keV) X-ray emission in nearby Compton-thick (CT) active galactic nuclei (AGN) extending out from the central supermassive black hole (SMBH) to ∼kiloparsec scales (e.g., Arévalo et al. 2014; Bauer et al. 2015; Fabbiano et al. 2017, 2018a, 2018b, 2019; Maksym et al. 2017; Jones et al. 2020) challenges the established picture that the characteristic hard X-ray continuum and fluorescent Fe Kα lines are confined to the nuclear surroundings, as would be expected in the standard model of an AGN enshrouded by a CT obscuring torus (e.g., Chou et al. 2007; Marinucci et al. 2012, 2017). The extended diffuse emission is not only detected in the direction of the ionization cones but also present in the region perpendicular to the ionization cones, i.e., cross-cones (e.g., Fabbiano et al. 2018a, 2018b, 2019; Jones et al. 2020), where the obscuring torus in the standard AGN unified model should completely obscure the nucleus (e.g., Antonucci 1993; Urry & Padovani 1995; Netzer 2015).

The spatial extent of the hard X-rays and the presence in both the ionization cones and cross-cones have several implications, linking the structure of the obscuring torus with the impact on the host galaxy, i.e., AGN feedback. First, measuring the amount of extended hard X-ray emission will help quantify potential bias in spectral modeling of the reprocessed emission from the torus (Baloković et al. 2014; Bauer et al. 2015; Farrah et al. 2016). Ignoring its presence will bias the spectral modeling of the AGN torus, as this emission will be incorrectly attributed to the torus, leading to biased estimates of the structural parameters of the torus, such as its covering factor. The presence of extended hard X-ray emission in the cross-cones indicates that the torus is likely porous. Second, the extent of hard X-ray emission suggests interaction of nuclear photons with the interstellar medium (ISM) of the host galaxy. The hard continuum and Fe Kα extended emission observed in ESO 428-G014, a well-studied nearby CT AGN, are likely caused by scattering off dense molecular clouds in the host galaxy of photons escaping the nuclear region (e.g., Fabbiano et al. 2017, 2018a, 2018b, 2019). The kiloparsec-scale spatial extent is larger at the lower energies, suggesting that the optically thick molecular clouds responsible for the scattering of the higher-energy photons are more concentrated in the inner radii. Finally, the fraction of CT AGN with extended hard emission will constrain the duty cycle for AGN feedback onto the host galaxy ISM.

Since there are only a handful of such detections so far, we need to build a statistical sample to answer the following questions: (1) Is the extended hard X-ray emission ubiquitous in CT AGN? (2) What is the typical extent and amount of extended hard X-ray emission relative to the total emission, and is there a limit on the physical scales that the extended hard X-ray can reach? (3) What is the origin of the extended hard X-ray emission and its implications on AGN models?

In an effort to address these questions, we have been conducting a Chandra survey of nearby ($z < 0.02$) CT AGN with joint NuSTAR observations. CT AGN have the advantage that the nuclear continuum emission is suppressed by CT obscuring materials such that the diffuse extended emission can be revealed. Chandra's combined subarcsecond resolution and sensitivity are essential for this study, as we can spatially resolve the extended component on <100 pc scales, quantitatively measure the extent and fraction of this component, and compare with optical, submillimeter, or radio observations to

investigate the origin. These measurements from the Chandra observations will provide constraints on torus parameters, e.g., opening angle and covering factor, and test the validity of torus modeling with the NuSTAR spectra.

In this paper, we present the results from our pilot Chandra ACIS survey of seven nearby CT AGN selected from the Swift-BAT spectroscopic AGN survey (Koss et al. 2017). We describe the sample selection, Chandra observations, and data reduction in Section 2. Section 3 introduces the spatial analysis methods we used in this work. We discuss our results in Section 4 and compare with other extended hard X-ray-detected CT AGN in the literature in Section 5. We also discuss implications for torus modeling and AGN feedback. We summarize the conclusions and implications for future observations in Section 6.

Throughout this paper, we adopt a concordance ΛCDM cosmological model with $H_0 = 70\,\mathrm{km\,s^{-1}\,Mpc^{-1}}$, $\Omega_\Lambda = 0.7$, and $\Omega_\mathrm{m} = 0.3$.

2. Sample Selection, Observations, and Data Reduction

The seven CT AGN are the targets of our pilot joint Cycle 20 Chandra and NuSTAR program (P.I. M. Elvis). They are drawn from the Swift-BAT spectroscopic AGN survey 70-month catalog (Koss et al. 2017), based on the following criteria. (1) We selected those with $z < 0.013$, $D < 50$ Mpc, which gives a plate scale of $1'' \sim 250$ pc, such that the extended emission can be spatially resolved with subarcsecond Chandra ACIS-S imaging. (2) We used a 2–10 keV BASS flux cut of $>4 \times 10^{-13}\,\mathrm{erg\,cm^{-2}\,s^{-1}}$ to ensure an adequate count rate. (3) We restricted the source list to those with X-ray spectra that indicate $\log N_\mathrm{H} > 10^{23.9}\,\mathrm{cm^{-2}}$ (Ricci et al. 2017).

Table 1 summarizes the Chandra observations used in this work. We first reprocessed the data using CIAO[4] (v4.12) and CALDB[5] (v4.9.0) (Fruscione 2006), provided by the Chandra X-ray Center (CXC). In addition to the Chandra Cycle 20 observations (ObsIDs 21417–21423), NGC 424 and 2MASX J00253292+6821442 (J0025+6821 hereafter) also have archival observations that can be merged and included in the analysis. We inspected each observation and made centroid shifts (Table 1), with the longer observation as the astrometric reference to better align the images. We merged the observations following the CIAO merge threads.[6,7] High background flares (3σ) were examined, and the entire data set was acceptable. Pileup is not a concern given the count rates and the (1/4) subarray configurations of our observations. PIMMS[8] estimates that the pileup fraction in ACIS-S is at most 1% for all except NGC 424, which has an acceptable pileup fraction of ∼3%.

3. Methods Used in Spatial Analysis

3.1. Subpixel Imaging and Adaptive Smoothing

We used the CIAO image analysis tools installed in SAOImage DS9[9] to investigate the X-ray morphological properties of the CT AGN. We created images in the 0.3–7.0 keV band (full band), the 0.3–3.0 keV band (soft band), the 3.0–7.0 keV band (hard band), and the 6.0–7.0 keV band (where the Fe Kα line dominates) if possible for the following analysis. We employed the subpixel binning technique to push for the highest spatial resolution, which has been tested and frequently applied to imaging studies of X-ray jets and extended emission (e.g., Wang et al. 2011a, 2011b, 2011c; Paggi et al. 2012). A fine pixel size of 0.″062 (1/8 of the ACIS native pixel size) was used when producing the images. We further generated adaptively smoothed images using *dmimgadapt*[10] to demonstrate morphological structures on different scales. The adaptively smoothed images were built from the 1/8 subpixel data using a 0.5–15 pixel scale with 5 counts under the kernel for 30 iterations. The smoothing parameters were chosen to optimize the details of the extended diffuse emission. Almost all the smoothed images reveal high surface brightness cores and large-scale, low surface brightness in the outer regions. The X-ray emission is more extended in the soft band; the hard X-ray emission is more concentrated in the center (Section 4).

3.2. Radial Profiles

To quantitatively measure the extent and amount of extended emission, we generated radial surface brightness profiles in different energy bands and different azimuthal sectors (when possible), following the procedure described in Fabbiano et al. (2017) (see also Fabbiano et al. 2018a; Jones et al. 2020). Concentric annuli were used to extract radial profiles out to a radius of 8″, reaching the background level. Off-nuclear point sources within the 8″-radius circle were all removed before generating the radial profiles. We started with an annular bin size of 0.″5 and increased the bin size at larger radii to maintain a minimum of 10 counts in each bin. To gauge the magnitude and significance of the extended emission, we compared the radial profiles to the Chandra point-spread functions (PSFs) for the corresponding energy bands. We modeled the PSF for each given centroid position and energy band using ChaRT[11] and MARX 5.5.0[12] following the CIAO PSF simulation thread.[13] The radial profile plots show the background-subtracted (measured from large off-source areas) surface brightness distribution in units of counts per arcsecond^2 in each energy band. The PSF radial profiles were generated in the same energy bands and were normalized to the counts in the central 0.″5-radius bin. To avoid potential contamination from a nuclear component, we focus on analyzing the region outside the central 1.″5-radius circle. Table 2 lists the excess counts over the Chandra PSF with associated Poisson statistical errors (including the background error), as well as the fraction of the extended emission in the 1.″5–8″ annular region in each energy band. The extended fraction is defined as the ratio of the excess counts above the Chandra PSF in the 1.″5–8″ annular region to the background-subtracted, total counts within the 8″-radius circle at the given energy band. We also list in Table 2 the excess counts within the central 1.″5 region, as some sources do not show excess emission beyond 1.″5. We define the total excess fraction to be the ratio of the total excess

[4] CIAO; http://cxc.harvard.edu/ciao/.
[5] CALDB; http://cxc.harvard.edu/caldb/.
[6] http://cxc.harvard.edu/ciao/threads/combine/
[7] https://cxc.harvard.edu/ciao/threads/merge_all/
[8] PIMMS v4.10; https://cxc.harvard.edu/toolkit/pimms.jsp.
[9] ds9; http://ds9.si.edu.
[10] https://cxc.harvard.edu/ciao/gallery/smooth.html
[11] https://cxc.harvard.edu/ciao/PSFs/chart2/
[12] https://space.mit.edu/cxc/marx
[13] https://cxc.cfa.harvard.edu/ciao/threads/psf.html

Table 1
Observation Log

Source Name	z	ObsID	Instrument	$T_{\rm exp}$ (ks)	PI	Date	dx (pixels)	dy (pixels)	Net Counts
NGC 424 (TOLOLO 0109-383)	0.01176	21417	ACIS-S	15.28	Elvis	2019 Feb 7	⋯	⋯	748 ± 28
		3146	ACIS-S	9.18	Matt	2002 Feb 4	−0.308	0.048	1238 ± 35
NGC 1125	0.01093	21418	ACIS-S	53.15	Elvis	2019 Oct 25	⋯	⋯	696 ± 27
NGC 3281	0.01067	21419	ACIS-S	9.13	Elvis	2019 Jan 24	⋯	⋯	431 ± 21
NGC 4500	0.01038	21420	ACIS-S	18.13	Elvis	2019 Aug 11	⋯	⋯	274 ± 17
ESO 005-G004	0.00623	21421	ACIS-S	21.94	Elvis	2019 Feb 18	⋯	⋯	189 ± 15
ESO 137-G034	0.0090	21422	ACIS-S	44.76	Elvis	2019 Oct 16	⋯	⋯	1119 ± 34
2MASX J00253292+6821442	0.0120	21423	ACIS-S	29.54	Elvis	2019 Oct 10	⋯	⋯	230 ± 16
		12862	ACIS-S	4.9	Mushotzky	2010 Dec 3	1.369	−1.327	53 ± 8

Note. dx and dy are the positional shifts relative to the reference image in the ACIS instrumental pixels (0.″492). The total counts at 0.3–7 keV above the background are listed in the last column.

Table 2
Excess Counts over the Chandra PSF, Extended Fractions, and Total Excess Fractions

Source Name	0.3–3.0 keV Excess Counts 1.″5–8″	0.3–3.0 keV Excess Counts ⩽1.″5	0.3–3.0 keV Total Excess Counts	0.3–3.0 keV Extended Fraction 1.″5–8″	0.3–3.0 keV Total Excess Fraction
NGC 424	85.1 ± 11.3 (7.5σ)	300.8 ± 22.5 (13.4σ)	385.9 ± 25.2 (15.3σ)	5.9% ± 0.8%	25.4% ± 1.9%
NGC 1125[a]	84.2 ± 10.9 (7.7σ)	131.3 ± 13.2 (10.0σ)	215.5 ± 17.1 (12.6σ)	22.8% ± 3.2%	58.4% ± 5.6%
NGC 1125[b]	155.8 ± 13.8 (11.3σ)	128.6 ± 13.1 (9.8σ)	284.4 ± 19.0 (14.9σ)	35.3% ± 3.6%	64.5% ± 5.4%
NGC 3281	41.4 ± 7.1 (5.9σ)	23.1 ± 5.2 (4.4σ)	64.5 ± 8.8 (7.3σ)	55.5% ± 11.6%	80.5% ± 15.0%
NGC 4500	33.2 ± 7.1 (4.7σ)	56.8 ± 8.1 (7.0σ)	90.0 ± 10.8 (8.4σ)	26.1% ± 6.1%	70.8% ± 10.8%
ESO 005-G004	8.4 ± 5.2 (1.6σ)	13.3 ± 4.7 (2.9σ)	14.4 ± 5.9 (2.4σ)	49.3% ± 35.6%	84.8% ± 46.1%
ESO 137-G034	341.1 ± 19.3 (17.7σ)	222.0 ± 15.8 (14.0σ)	563.2 ± 25.0 (22.6σ)	49.4% ± 3.3%	81.6% ± 4.8%
J0025+6821	8.6 ± 5.4 (1.6σ)	12.4 ± 5.4 (2.3σ)	18.0 ± 6.9 (2.6σ)	15.9% ± 10.4%	33.3% ± 13.9%
	3.0–7.0 keV excess counts 1.″5–8″	3.0–7.0 keV excess counts ⩽1.″5	3.0–7.0 keV total excess counts	3.0–7.0 keV extended fraction 1.″5–8″	3.0–7.0 keV total excess fraction
NGC 424	<15.9	88.5 ± 14.3 (6.2σ)	65.9 ± 15.3 (4.3σ)	<2.9%	12.1% ± 2.9%
NGC 1125[a]	<18.3	32.7 ± 9.7 (3.4σ)	38.2 ± 11.5 (3.3σ)	<7.7%	16.1% ± 5.0%
NGC 1125[b]	23.5 ± 7.5 (3.1σ)	23.8 ± 9.4 (2.5σ)	47.3 ± 12.0 (3.9σ)	9.2% ± 3.0%	18.5% ± 4.9%
NGC 3281	12.0 ± 6.2 (1.9σ)	36.1 ± 11.0 (3.3σ)	48.1 ± 12.6 (3.8σ)	3.4% ± 1.8%	13.5% ± 3.6%
NGC 4500	<12.2	22.4 ± 7.7 (2.9σ)	21.5 ± 8.4 (2.6σ)	<8.3%	14.6% ± 5.9%
ESO 005-G004	7.3 ± 4.9 (1.5σ)	22.1 ± 7.9 (2.8σ)	29.5 ± 9.3 (3.2σ)	4.3% ± 2.8%	17.1% ± 5.5%
ESO 137-G034	33.1 ± 8.4 (3.9σ)	62.1 ± 12.4 (5.0σ)	95.2 ± 15.0 (6.4σ)	7.7% ± 2.0%	22.2% ± 3.7%
J0025+6821	5.4 ± 5.3 (1.0σ)	11.8 ± 8.2 (1.4σ)	17.1 ± 9.8 (1.7σ)	2.4% ± 2.3%	7.5% ± 4.3%
	6.0–7.0 keV excess counts 1.″5–8″	6.0–7.0 keV excess counts ⩽1.″5	6.0–7.0 keV total excess counts	6.0–7.0 keV extended fraction 1.″5–8″	6.0–7.0 keV total excess fraction
ESO 137-G034	8.7 ± 4.7 (1.9σ)	25.3 ± 8.0 (3.2σ)	34.0 ± 9.3 (3.7σ)	5.1% ± 2.8%	20.1% ± 5.7%
	0.3–7.0 keV excess counts 1.″5–8″	0.3–7.0 keV excess counts ⩽1.″5	0.3–7.0 keV total excess counts	0.3–7.0 keV extended fraction 1.″5–8″	0.3–7.0 keV total excess fraction
NGC 424	92.6 ± 12.5 (7.4σ)	423.4 ± 26.7 (15.9σ)	516.0 ± 27.7 (18.6σ)	4.7% ± 0.6%	24.6% ± 1.6%
NGC 1125[a]	94.8 ± 12.5 (7.6σ)	171.9 ± 16.3 (10.5σ)	266.7 ± 20.6 (13.0σ)	15.6% ± 2.2%	44.0% ± 3.9%
NGC 1125[b]	184.7 ± 15.7 (11.7σ)	160.6 ± 16.1 (10.0σ)	345.3 ± 22.5 (15.3σ)	26.5% ± 2.5%	49.6% ± 3.8%
NGC 3281	59.5 ± 9.4 (6.3σ)	69.9 ± 12.0 (5.8σ)	129.4 ± 15.2 (8.5σ)	13.8% ± 2.3%	30.0% ± 3.8%
NGC 4500	37.7 ± 8.2 (4.6σ)	83.9 ± 10.9 (7.7σ)	121.6 ± 13.7 (8.9σ)	13.8% ± 3.1%	44.4% ± 5.7%
ESO 005-G004	16.8 ± 7.1 (2.3σ)	31.3 ± 8.3 (3.8σ)	48.1 ± 11.0 (4.4σ)	8.9% ± 3.8%	25.4% ± 6.1%
ESO 137-G034	384.2 ± 21.1 (18.1σ)	302.9 ± 20.0 (15.1σ)	687.1 ± 29.1 (23.6σ)	34.3% ± 2.2%	61.4% ± 3.2%
J0025+6821	15.2 ± 7.6 (2.0σ)	21.8 ± 9.3 (2.4σ)	37.1 ± 12.0 (3.1σ)	5.4% ± 2.7%	13.1% ± 4.3%

Notes. Extended fraction ≡ (Source 1.″5–8″ counts − PSF 1.″5–8″ counts)/(Total 8″ source counts). Total excess fraction ≡ (Source 0.″5–8″ counts − PSF 0.″5–8″ counts)/(Total 8″ source counts). We place a 3σ upper limit if there are no excess counts above the PSF (i.e., <1σ).
[a] The two nearby X-ray sources are removed from the measurements.
[b] The two nearby X-ray sources are included in the measurements.

counts above the PSF (including the 0.″5–1.″5 region) to the total net counts within the 8″-radius circle at the given energy band. This includes all the extended emission that does not belong to the central point source.

In cases where we were able to identify azimuthal sectors, e.g., ionization cones and cross-cones, we also produced radial profiles in each cone region out to 8″, following the same procedure described above.

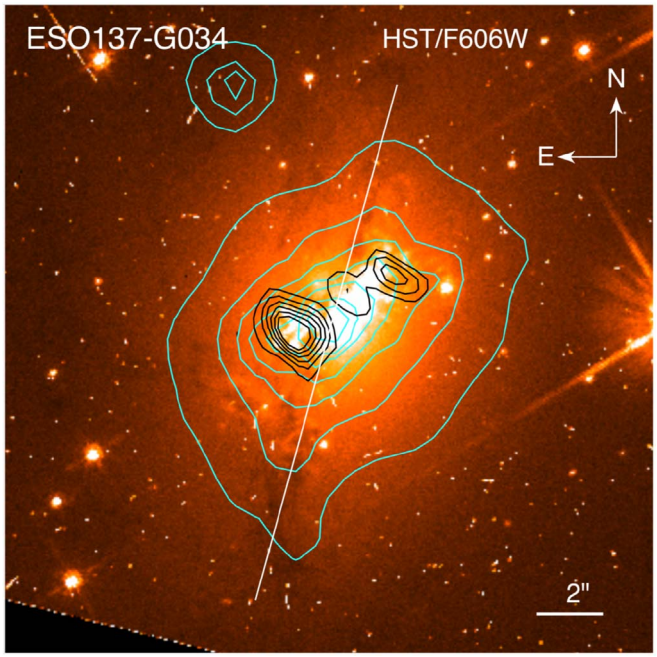

Figure 1. 20″ × 20″ HST/F606W image of ESO 137-G034 (Malkan et al. 1998), an S0/a galaxy hosting a Seyfert 2 nucleus. The Chandra 0.3–7.0 keV X-ray contours are overlaid in cyan, extending to the host galaxy out to 8″ in radius. The black contours are extracted from the ATCA radio map at 8.6 GHz in Morganti et al. (1999). There is a long dust lane passing close to the nucleus, parallel to the photometric major axis (P.A. ∼ 165°; white line) of the galaxy.

We discuss the morphology, extended component, and radial profiles of individual sources in the following section.

4. Results

4.1. ESO 137-G034

ESO 137-G034 is an S0/a galaxy (Figure 1; Malkan et al. 1998; Ferruit et al. 2000) hosting a Seyfert 2 nucleus at $z = 0.009$ ($D \sim 38.8$ Mpc; $1'' \sim 185$ pc) with a CT column density of $\log N_{\rm H} = 24.3$–$24.5\,{\rm cm}^{-2}$ (Ricci et al. 2015, 2017; Georgantopoulos & Akylas 2019). There is a long dust lane passing close to the nucleus, parallel to the photometric major axis of the galaxy.

4.1.1. Extended Soft X-Ray and Optical Line Emission

Figure 2 (top) shows the Chandra 0.3–3 keV soft-band and 3–7 keV hard-band images of ESO 137-G034 at 1/8 subpixel binning, and the adaptively smoothed versions are shown in the bottom row. ESO 137-G034 has the most prominent extended X-ray emission among the seven CT AGN. The soft-band emission is clearly seen as extended and elongated along the northwest–southeast (NW–SE) direction, while less extended along the northeast–southwest (NE–SW) direction. Based on the azimuthal dependence, we divided the data into two biconical regions opening ∼90° outward from the central nucleus in the NW–SE direction (i.e., ionization cones) and in the NE–SW direction (i.e., cross-cones). The ionization bicone axis is oriented ∼130° measured from north through east. We generated radial profiles over all azimuthal angles (Figure 3) and in the ionization cones and cross-cones defined above (Figure 4). To assess the significance of the extended emission, we measured the excess counts over the PSF in all the cone regions and calculated the extended fractions both in the bicone regions and in the 8″-radius circular region (Table 2). Figures 3 and 4 show that the soft X-ray emission has excess counts above the PSF at all radii in all the cone and cross-cone regions. About half of the total, background-subtracted counts at 0.3–3.0 keV are in the extended component (i.e., 1.″5–8″ annular region), with ∼40% in the ionization cones and ∼10% in the cross-cones. The diffuse soft X-ray component extends to at least 8″ (∼1.5 kpc) in radius in the ionization cone direction.

Previous Hubble Space Telescope (HST) optical [O III] λ5007 and Hα line maps show a similar morphology to the soft X-ray emission in the inner 4″-radius region, although more detailed structures are revealed in the optical line maps (Ferruit et al. 2000). Outside the 4″-radius region, instead of further extending along the NW–SE direction, the optical line emission displays extended tails at the extreme north and south ends of the emission-line region, forming a Z-shaped morphology (see Figure 21 in Ferruit et al. 2000). Our Chandra data also show this pattern in the soft X-ray emission of further extended tails to the north and south out to ∼8″ measured from the center. This would not be surprising, as previous studies already show a strong morphological correlation between the extended soft X-ray associated with AGN and extended [O III] emission, likely due to a single photoionized medium giving rise to both the [O III] and soft X-rays (e.g., Bianchi et al. 2006; Levenson et al. 2006; Koss et al. 2015). More recent studies suggest that the ionized medium is more complex, and this correlation is due to some combination of photoionization and collisional excitation in a multiphase medium (e.g., Paggi et al. 2012; Maksym et al. 2017, 2019). Ferruit et al. (2000) reported an integrated [O III] λ5007 line flux of $6.5 \times 10^{-13}\,{\rm erg\,cm^{-2}\,s^{-1}}$ in a 14″ × 22″ extraction box around the entire line-emitting region. We measured the integrated flux of the soft X-ray emission (using *srcflux* in CIAO) in the same extraction box to be $f_{0.5-2\,{\rm keV}} = (1.4 \pm 0.1) \times 10^{-13}\,{\rm erg\,cm^{-2}\,s^{-1}}$. The [O III]/soft X-ray flux ratio of the integrated emission is ∼4.8, which is very similar to the ratios of other Seyfert CT AGN that also have Chandra and HST observations, e.g., NGC 3393 and Mrk 3 (Bianchi et al. 2006). Our Chandra data are not deep enough, though, to allow us to examine the variations of the [O III]/soft X-ray ratio cloud by cloud or radially as a function of distance from the nucleus as in, e.g., NGC 4151 (Wang et al. 2011a, 2011b, 2011c) and Mrk 573 (Paggi et al. 2012).

The Z-shaped structure of high-excitation gas surrounds a three-component radio structure as observed with the Australia Telescope Compact Array (ATCA) at 8.6 GHz (Figure 1; Morganti et al. 1999), coincident with the inner part of the line-emitting gas. Deeper Chandra data are necessary to reveal whether there are tails and enable a comparison of the detailed structures of the X-rays, optical line emission, and radio emission.

4.1.2. Extended Hard X-Ray Emission

ESO 137-G034 displays the most prominent extended hard X-ray emission among the seven CT AGN, with an excess of 33.1 ± 8.4 counts over the PSF at 3–7 keV and an extended fraction of 7.7% in the 1.″5–8″ region (Table 2). Almost all of the excess counts come from the ionization bicone with a 3.7σ detection and a 5.6% extended fraction (Table 3). The inner 1.″5 region also has significant excess emission detected at

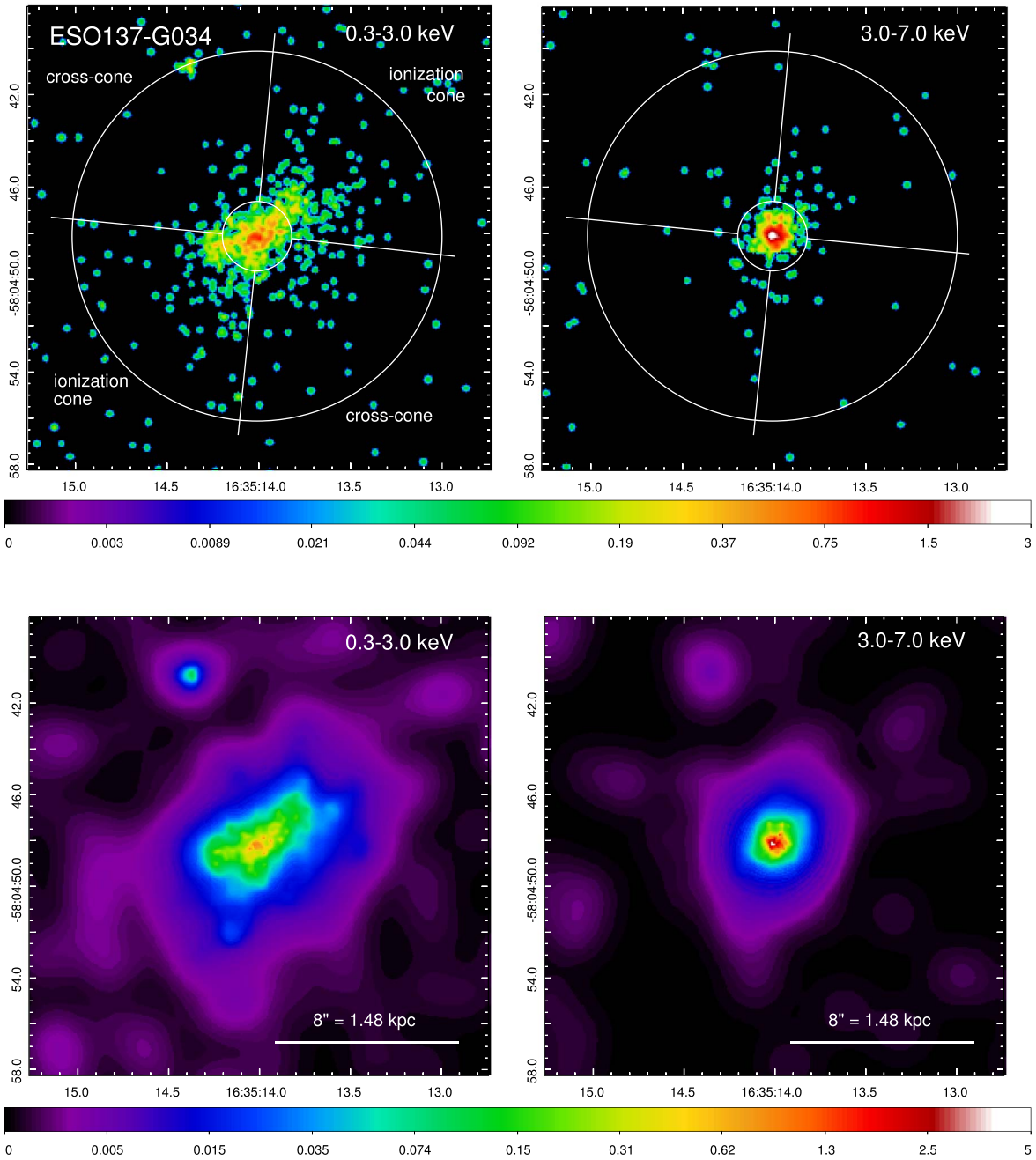

Figure 2. Top: $20'' \times 20''$ Chandra ACIS-S 0.3–3.0 keV (left) and 3.0–7.0 keV (right) band images of ESO 137-G034 at 1/8 subpixel binning. Based on the azimuthal dependence of the soft X-ray emission, the $8''$-radius circular region is divided into the NW–SE ionization cones with an opening angle of 90° and the NE–SW cross-cones. The ionization bicone axis is oriented ∼135° measured from north through east. The inner $1\farcs5$-radius circle and the outer $8''$-radius circle define the region in between for extracting excess counts in the extended emission. Bottom: adaptively smoothed images (*dmimgadapt*; 0.5–15 pixel scales, 5 counts under kernel, 30 iterations) on 1/8 binned pixel. All the images are displayed in logarithmic scale, with colors corresponding to the counts per image pixel.

$\sim 5\sigma$, contributing to a total of 95.2 ± 15.0 excess counts above the PSF and a total excess fraction of 22.2%, the highest fraction among the sample. The total extent of the diffuse hard X-ray emission is about $10''$ in diameter, or 1.85 kpc, which is roughly half the size of the extended soft X-ray emission.

The 6.0–7.0 keV band, where the Fe Kα line dominates, has a tentative $\sim 2\sigma$ detection of 5.1% extended emission with an excess of 8.7 ± 4.7 counts over the PSF in the $1\farcs5$–$8''$ region. The total excess counts, 34.0 ± 9.3, are better detected at above 3σ, accounting for ∼20% of the total emission owing to the contribution from the inner $1\farcs5$ region. The surface brightness (Figure 3) lies above the PSF out to $8''$ in radius, but we need deeper Chandra data to get a higher signal-to-noise ratio to confirm the total extent of this component.

4.2. NGC 3281

NGC 3281 is morphologically classified as an SAab galaxy (Figure 5) at $z = 0.01067$ ($D \sim 46.1$ Mpc; $1'' \sim 219$ pc). It hosts a Seyfert 2 nucleus with a CT column density of log $N_{\rm H} = 23.9$–$24.3\ {\rm cm}^{-2}$ (Vasylenko et al. 2013; Baloković 2017; Ricci et al. 2017).

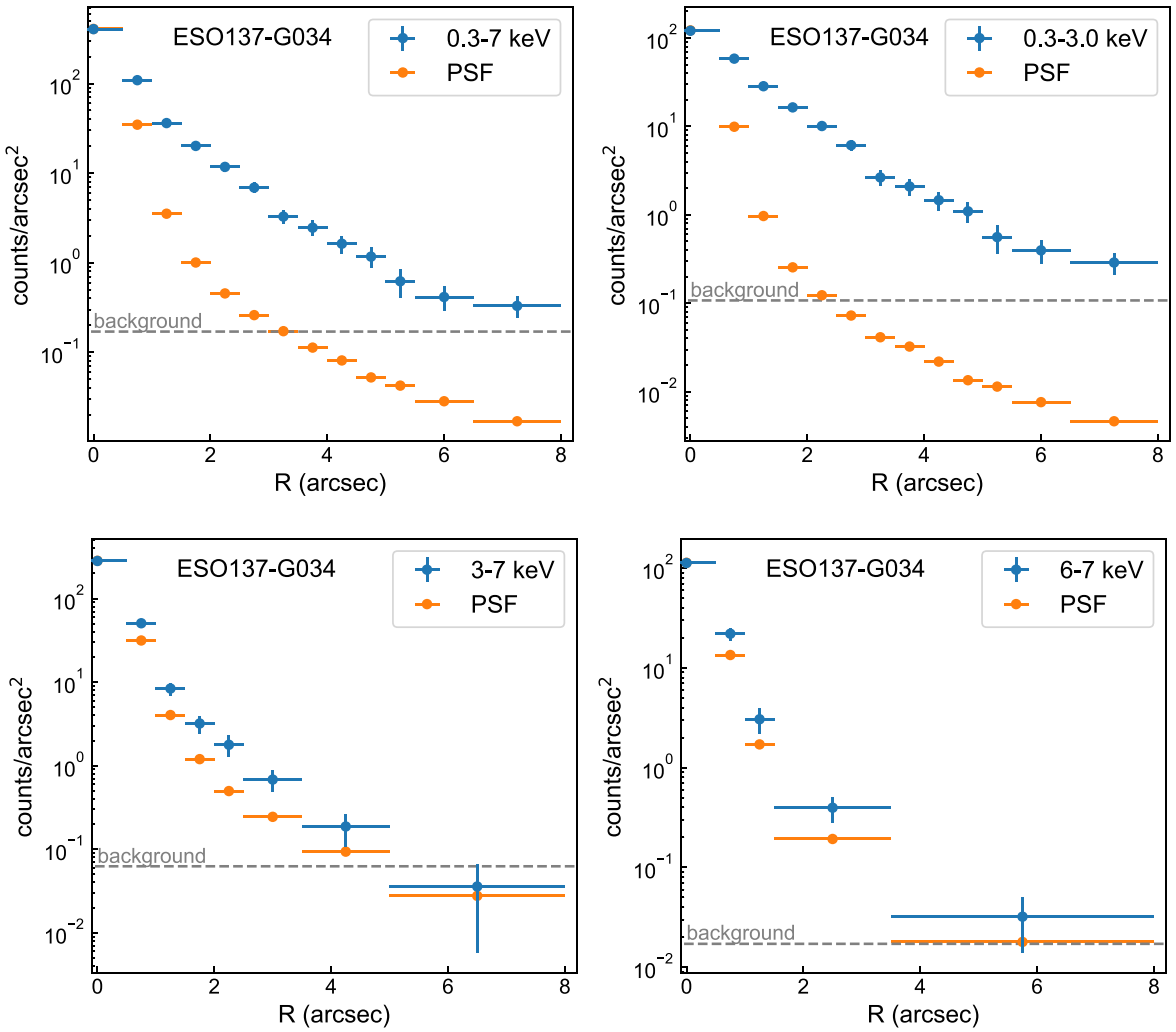

Figure 3. Radial profiles of ESO 137-G034 for the full energy band (0.3–7.0 keV), soft band (0.3–3.0 keV), hard band (3.0–7.0 keV), and the 6–7 keV band, where Fe Kα line dominates. The background has been subtracted off from the radial profiles, the level of which is indicated as the gray dashed horizontal line. The PSF is normalized to the counts in the central 0.″5-radius bin. We find excess emission above the PSF outside the nuclear region (0.″5, 93 pc) in all the energy bands.

Figure 6 shows that NGC 3281 has a relatively low surface brightness core in the soft band, and the soft X-ray emission is elongated and distributed asymmetrically along the N–S direction, with a larger northern extent ($\sim$8″, 1.8 kpc) than southern ($\sim$4″, 0.9 kpc). There is barely any emission in the perpendicular E–W direction. The hard X-ray band has a concentrated surface brightness distribution in the center and also has a vertically distributed, extended diffuse component, although less prominent than the soft X-rays. Since the X-ray emission has a strong azimuthal dependence in both the soft and hard bands, we split the data into two biconical regions with the bicone axis at a position angle of $\sim$178° east of north: one in the N–S direction (i.e., ionization cones) with a half-opening angle of $\sim$39°, and one in the E–W direction (i.e., cross-cones). We generated radial profiles in both the 8″ circular region and the cone regions defined above (Figures 7 and 8). The extended hard X-ray emission is detected at 3.2σ over the PSF with an extended fraction of 9.7% in the ionization bicone and a physical extent of $\sim$3.5 kpc in diameter (Table 4). No extended emission is detected along the direction of the cross-cones. Overall there are 48.1 $\pm$ 12.6 excess counts above the PSF at 3–7 keV, taking 13.5% of the total counts in this band.

NGC 3281 is one of the Seyfert galaxies selected in an HST survey of extended [O III] λ5007 emission by Schmitt et al. (2003a, 2003b). The [O III] line map displays a conically shaped narrow-line region preferentially distributed highly asymmetrically toward the N–E direction extending up to $\sim$1.3 kpc (see Figure 9 in Schmitt et al. 2003a), overlapping with the Chandra X-ray emission. Schmitt et al. (2003a) also noted that the ground-based observations by Storchi-Bergmann et al. (1992) showed more extended emission in the NE direction (up to 2 kpc from the disk), and the less extended emission from HST could be due to the relatively small field of view ($\sim$13″ in diameter) of the ramp filter. The lack of [O III] emission and also X-ray emission in the south is most likely caused by obscuration of the dust lanes in the host galaxy disk as seen in Figure 5. We measured the integrated soft X-ray flux, $f_{0.5-2\,\mathrm{keV}} = (1.1 \pm 0.3) \times 10^{-13}$ erg cm^{-2} s^{-1}, and used the [O III] line flux of 2.5×10^{-13} erg cm^{-2} s^{-1} in Schmitt et al. (2003a) to calculate the [O III]/soft X-ray ratio. The flux ratio of $\sim$2.3 is comparable to typical ratios of Seyfert galaxies (Bianchi et al. 2006).

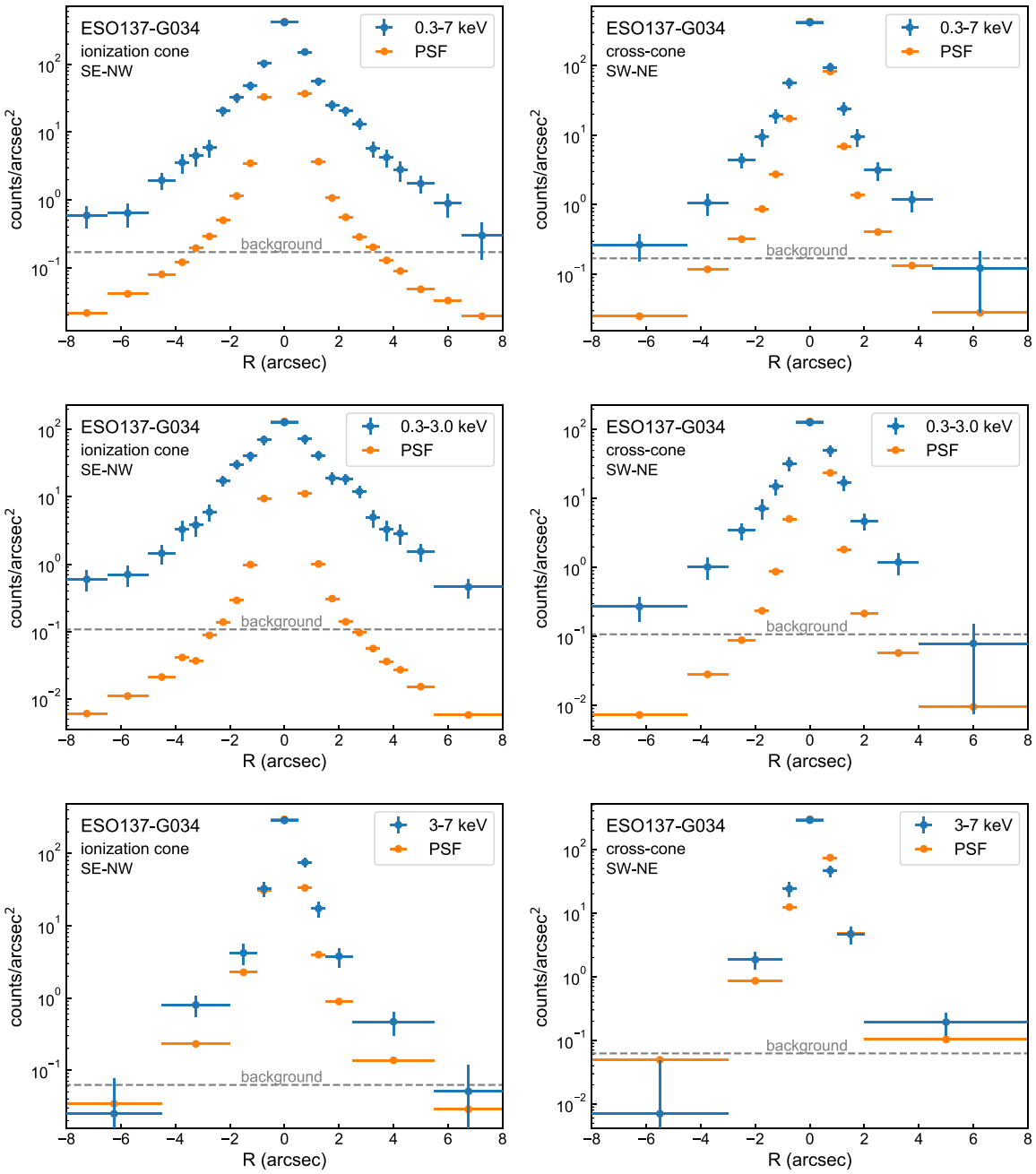

Figure 4. Radial profiles of ESO 137-G034 in the ionization and cross-cones for the full band, soft band, and hard band. The background has been subtracted off from the radial profiles, the level of which is indicated as the gray dashed horizontal line. The PSF is normalized to the counts in the central 0.″5-radius bin. The extended soft X-ray emission is well detected in both the ionization cones and the cross-cones, while the hard X-ray emission is only detected in the ionization cones.

4.3. NGC 424

NGC 424 is an SB0/a galaxy at $z = 0.01176$ ($D \sim 50.8$ Mpc; $1'' \sim 241$ pc). The nuclear activity is classified as Seyfert 1/Seyfert 2 with a CT column density of $\log N_{\rm H} = 24.1$–$24.3\ {\rm cm}^{-2}$ (Ricci et al. 2015, 2017; Paltani & Ricci 2017). Baloković et al. (2014) suggest that $N_{\rm H}$ could be even higher.

The Chandra 0.3–3.0 keV band image (Figure A1) shows a very high surface brightness in the central region, with the extended emission tending to distribute more along the E–W direction. NGC 424 is the only CT AGN in the sample that contains a higher central surface brightness core in the soft X-ray band than in the hard band. While the soft band has excess emission over the PSF at all radii (up to 8″, 1.9 kpc), the hard-band surface brightness drops quickly to the level of the PSF beyond 1.″0 (Figure A2). Although there is no extended hard X-ray emission detected beyond 1.″5, the inner 1.″5 region (up to ∼362 pc in radius) does show significant excess counts detected at 6.2σ above the PSF (Table 2). Overall the excess counts take up 13.5% of the total counts in the 3–7 keV band.

4.4. NGC 1125

NGC 1125 is an SB0/a galaxy (Figure 9) at $z = 0.01093$ ($D \sim 47.2$ Mpc; $1'' \sim 224$ pc), containing a Seyfert 2 nucleus

Table 3
ESO 137-G034: The Excess Counts over the Chandra PSF, Extended Fractions, and Total Excess Fractions in the NW–SE Ionization and NE–SW Cross-cones

Energy (keV)	NW–SE Ionization Cone Excess Counts 1.″5–8″	NW–SE Ionization Cone Excess Counts ⩽1.″5	NW–SE Ionization Cone Extended Fraction 1.″5–8″	NW–SE Ionization Cone Total Excess Fraction
0.3–3.0	271.6 ± 16.9 (16.1σ)	149.7 ± 12.8 (11.7σ)	39.4% ± 2.9%[a], 55.0% ± 4.2%[b]	61.1% ± 3.9%[a], 85.3% ± 5.8%[b]
3.0–7.0	23.9 ± 6.5 (3.7σ)	42.7 ± 9.4 (4.6σ)	5.6% ± 1.5%, 10.2% ± 2.9%	15.6% ± 2.8%, 28.4% ± 5.2%
6.0–7.0	5.9 ± 3.6 (1.6σ)	20.4 ± 6.3 (3.2σ)	3.5% ± 2.2%, 5.9% ± 3.7%	15.5% ± 4.4%, 26.2% ± 7.7%
0.3–7.0	299.8 ± 18.1 (16.5σ)	205.5 ± 15.9 (12.9σ)	26.8% ± 1.8%, 41.0% ± 2.9%	45.2% ± 2.6%, 69.0% ± 4.2%
Energy (keV)	NE–SW cross-cone excess counts 1.″5–8″	NE–SW cross-cone excess counts ⩽1.″5	NE–SW cross-cone extended fraction 1.″5–8″	NE–SW cross-cone total excess fraction
0.3–3.0	65.9 ± 8.9 (7.4σ)	60.0 ± 8.9 (6.7σ)	9.6% ± 1.3%[c], 33.8% ± 5.2%[d]	18.3% ± 2.0%[c], 64.5% ± 8.0%[d]
3.0–7.0	7.8 ± 5.0 (1.5σ)	<21.8	1.8% ± 1.2%, 4.0% ± 2.7%	<6.2%, <13.8%
6.0–7.0	<8.6	<13.1	<5.0%, <12.4%	<9.3%, <22.9%
0.3–7.0	78.5 ± 10.3 (7.6σ)	62.4 ± 11.4 (5.5σ)	7.0% ± 0.9%, 20.4% ± 2.9%	12.6% ± 1.4%, 36.5% ± 4.4%

Notes. We place a 3σ upper limit if there are no excess counts above the PSF (i.e., <1σ).
[a] The first fraction is the excess counts in the extended region of the NW–SE ionization bicone relative to the total counts within the 8″-radius circle at the given energy band.
[b] The second fraction is the excess counts in the extended region of the NW–SE ionization bicone relative to the total counts in the bicone itself at the given energy band.
[c] The first fraction is the excess counts in the extended region of the NE–SW cross-cones relative to the total counts within the 8″-radius circle at the given energy band.
[d] The second fraction is the excess counts in the extended region of the NE–SW cross-cones relative to the total counts in the cross-cones at the given energy band.

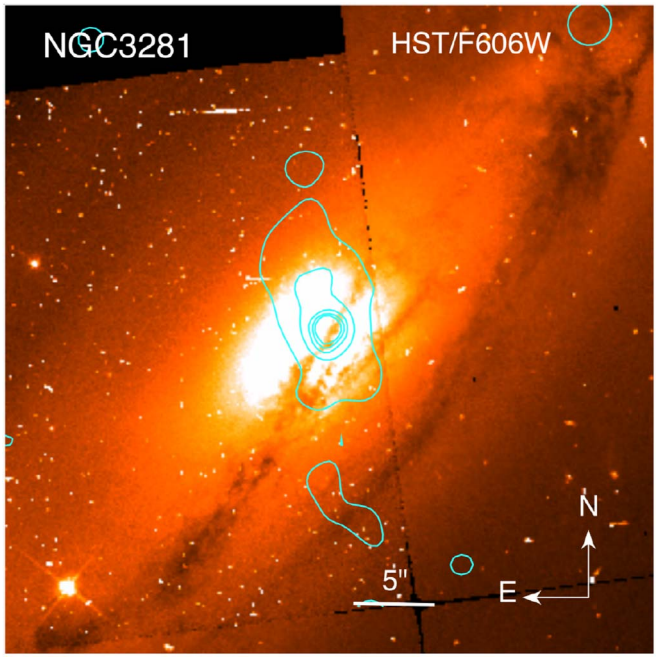

Figure 5. 40″ × 40″ HST/F606W image of NGC 3281 (Malkan et al. 1998), an SAab galaxy hosting a Seyfert 2 nucleus. The Chandra 0.3–3.0 keV X-ray contours are overlaid in cyan.

(Véron-Cetty & Véron 2006) with a CT column density of log $N_{\rm H}$ = 24.2–24.3 cm^{-2} (Ricci et al. 2015, 2017).

The Chandra data (Figure A3) exhibit an elongated morphology along the NW–SE direction in both the soft and hard bands, extending perpendicular to the major axis of the host galaxy shown in Figure 9. There are two X-ray sources detected off-center, but they have no optical counterparts in the HST/F606W image (Figure 9). We estimated their 0.3–7 keV X-ray luminosities to be ∼3 × 10^{39} erg s^{-1} and ∼3 × 10^{38} erg s^{-1}, which suggest that they could be high-mass X-ray binaries within the NGC 1125 host galaxy. However, we cannot completely rule out the possibility that these two blobs are part of an ionization cone structure.

Figure A4 shows the radial profiles extracted after subtracting the two sources. The extended emission is well detected in the soft X-ray band, with a physical scale of ∼1.8 kpc in radius. While the surface brightness of the hard X-ray emission lies above the PSF out to ∼5″ (∼1.1 kpc) in radius, the measured excess counts in the 1.″5–8″ region are negligible compared to the statistical error. The inner 1.″5 region does show excess counts above the PSF at >3σ, making a total excess fraction of 16.1%. We also extracted excess counts including the two sources (Table 1), which would make the 3–7 keV band a 3σ detection in the extended emission.

4.5. NGC 4500

NGC 4500 is an SBa galaxy at z = 0.01038 (D ∼ 44.8 Mpc; 1″ ∼ 213 pc). The optical morphology is similar to that shown by Seyfert galaxies with a dominant bright, star-like nucleus. But the nuclear activity can be explained by a starburst, and NGC 4500 is classified as having a starburst nucleus or a composite AGN (Balzano 1983; Koss et al. 2017) with log $N_{\rm H}$ = 23.9 cm^{-2} (Ricci et al. 2017).

Figure A5 shows that the X-ray emission appears to be preferentially distributed along the N–S direction in both the soft and hard bands, especially toward the north. The soft X-ray emission extends to 4.″5 (∼1 kpc) in radius. The extended component in the hard band is not detected in the 1.″5–8″ annular region. The radial profiles (Figure A6) do show some excess emission in the hard band out to 2″ (∼426 pc), with a total of 21.5 excess counts over the PSF and a total excess fraction of 14.6%, although not statistically significant.

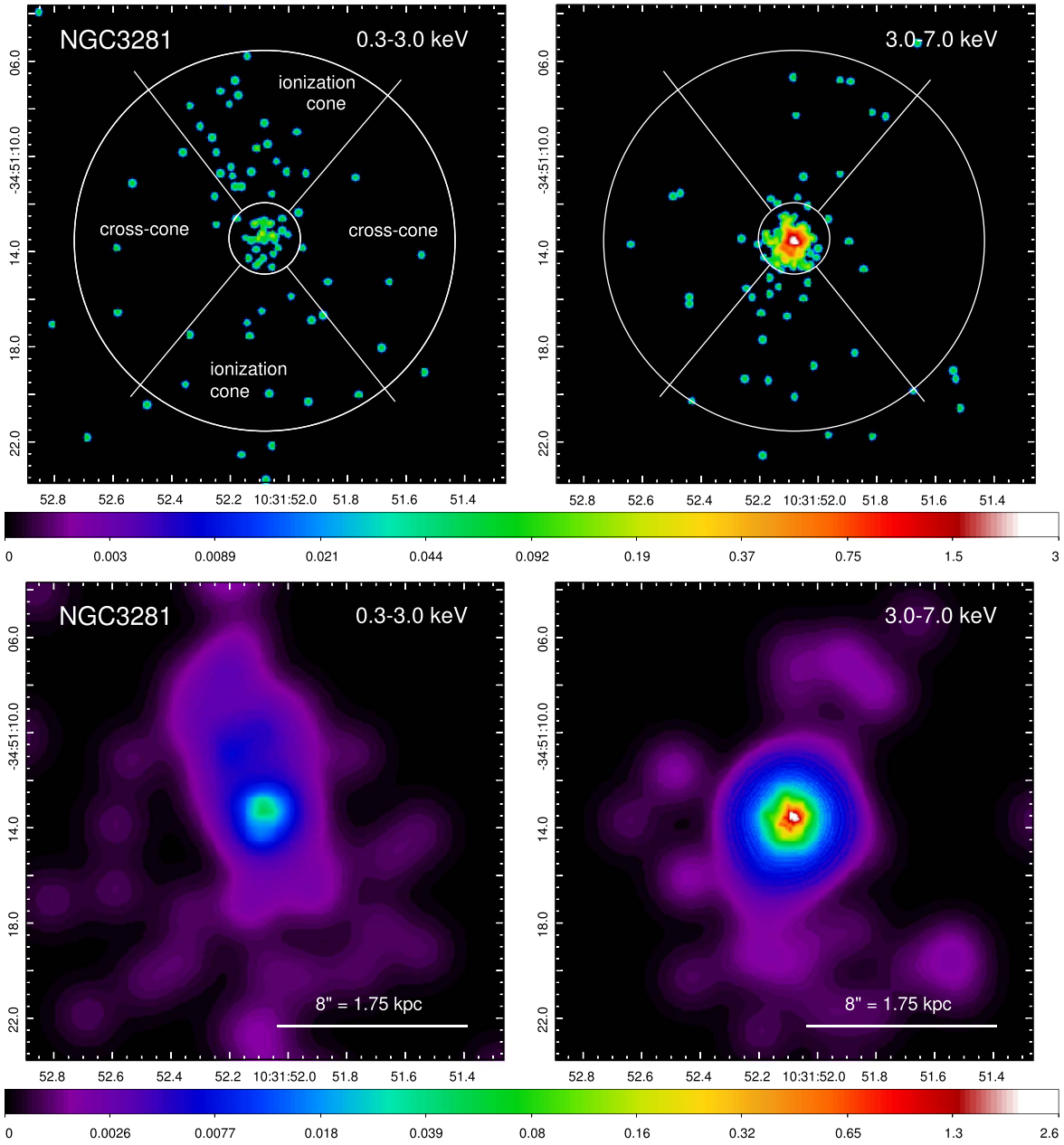

Figure 6. Top: $20'' \times 20''$ Chandra ACIS-S 0.3–3.0 keV (left) and 3.0–7.0 keV (right) band images of NGC 3281 at 1/8 subpixel binning. The inner $1\farcs5$-radius circle and the outer $8''$-radius circle define the region in between for extracting excess counts in the extended emission. Given the azimuthal dependence of the soft and hard X-ray emission, the $8''$-radius circular region is split into the N–S ionization cones with a half-opening angle of 39° and the E–W cross-cones. The X-ray bicone axis is at a position angle of ∼178° east of north. Bottom: adaptively smoothed images (*dmimgadapt*; 0.5–15 pixel scales, 5 counts under kernel, 30 iterations) on 1/8 binned pixel. All the images are displayed in logarithmic scale, with colors corresponding to the counts per image pixel.

4.6. ESO 005-G004

ESO 005-G004 is an Sb edge-on galaxy hosting a Seyfert 2 nucleus at $z = 0.00623$ ($D \sim 26.8$ Mpc; $1'' \sim 128$ pc) with a CT column density of log $N_{\rm H} = 24.2$–$24.3\ {\rm cm}^{-2}$ (Ricci et al. 2015, 2017; Baloković 2017).

As shown in Figure A7, the extended soft X-ray emission is not detected in ESO 005-G004, without any concentrated emission in the center. This extremely low level of soft X-ray emission is likely due to high column density absorption in the disk of the host galaxy in an edge-on view. A high surface brightness core appears in the hard band, and the radial profile (Figure A8) shows excess emission out to at least $3''$ (384 pc) in radius with a total of 29.5 ± 9.3 excess counts above the PSF, taking up 17.1% of the total counts.

4.7. 2MASX J00253292+6821442

J0025+6821 is a Seyfert 2 galaxy (morphology not classified) at $z = 0.0120$ ($D \sim 51.9$ Mpc; $1'' \sim 246$ pc) with a column density of log $N_{\rm H} = 23.9$–$24.3\ {\rm cm}^{-2}$ (Baloković 2017; Ricci et al. 2017).

This source also has a low level of soft X-ray emission (Figure A9), and the extended component is not detected above 3σ. The surface brightness of the hard X-ray emission is concentrated in the center and then quickly drops to the PSF

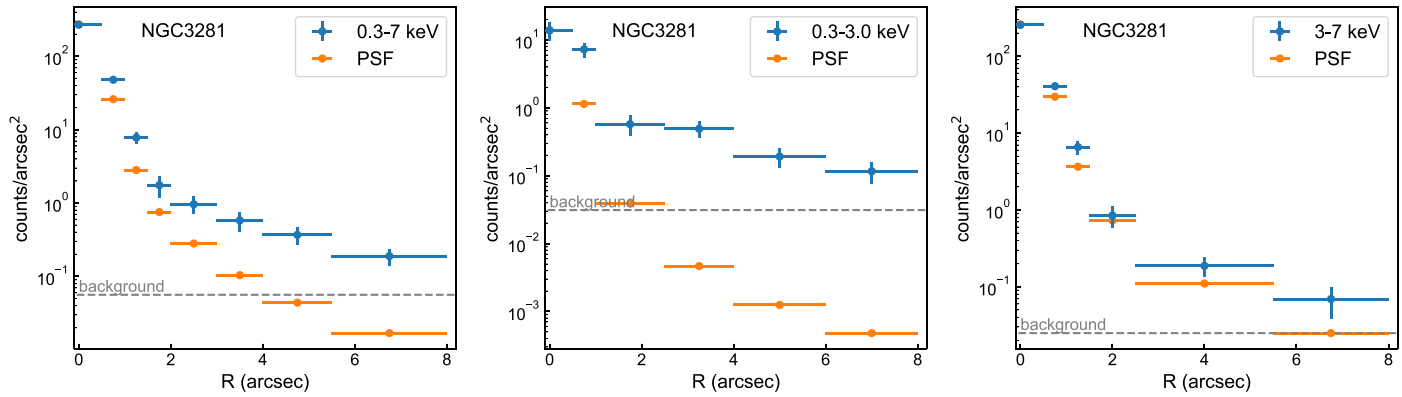

Figure 7. Radial profiles of NGC 3281 for the full band, soft band, and hard band. The background has been subtracted off from the radial profiles, the level of which is indicated as the gray dashed horizontal line. The PSF is normalized to the counts in the central 0.″5-radius bin.

level (Figure A10). No extended emission is detected in the hard band either.

5. Discussion

5.1. Comparison with Extended Hard-X-Ray-detected Sources in the Literature

So far, only a handful of sources in the literature have detections of extended hard X-ray emission (e.g., Circinus, Arévalo et al. 2014; NGC 1068, Bauer et al. 2015), and ESO 428-G014 (Fabbiano et al. 2017, 2018a, 2018b) and NGC 7212 (Jones et al. 2020) exhibit prominent, kiloparsec-scale hard X-ray emission. For ESO 428-G014 and NGC 7212, both the 3–6 keV hard X-ray continuum and Fe Kα show extended emission out to 15″ and 8″, corresponding to ∼1.8 and ∼4.3 kpc in radius, respectively. Unlike the seven CT AGN in this relatively shallow pilot survey, ESO 428-G014 and NGC 7212 have comparable, deep cumulative Chandra exposures of 154 and 150 ks and a similar total number of 1554 and 1529 counts in the 3–7 keV band (hence similar count rates), although the distances or physical scales (per arcsec) differ by a factor of 4.6. We extracted the excess counts and measured the extended fractions and total excess fractions in the 3–7 keV and 6–7 keV bands for ESO 428-G014 and NGC 7212 in the same manner as our seven CT AGN (Table 5). For ESO 428-G014, the excess emission at 3–7 keV in the extended 1.″5–8″ region is well detected above the PSF at 16σ, contributing 20.8% of the total emission in this band. Adding the excess counts in the inner 0.″5–1.″5 region, we measured a total of 462.9 ± 31.3 excess counts above the PSF and a total excess fraction of 30.2%. The 6–7 keV band (Fe Kα) also shows significant extended emission with a total of 72.8 ± 16.2 excess counts above the PSF, accounting for 16.4% of the total emission in this band. For NGC 7212 (the most distant source among the nine CT AGN), the excess counts in the extended 1.″5–8″ region are also well detected above the PSF with an extended fraction of 14.7%. The total excess counts, 549.5 ± 23.4, make up 35.7% of the total emission at 3–7 keV, the highest fraction reported so far. The extended emission is also prominent in the 6–7 keV band, with a total of 95.7 ± 9.8 excess counts above the PSF and a total excess fraction of 25.5%.

ESO 428-G014 and NGC 7212 bookend the redshift/distance range of our seven CT AGN, most of which are at $z \sim 0.01$. Five out of seven CT AGN in our sample show total excess emission in the 3–7 keV band ranging from ∼12% to 22% that are >3σ detections. Among the seven CT AGN, ESO 137-G034 and NGC 3281 are the only two that display biconical ionization structures, and their extended 3–7 keV emission is well detected above 3σ along the ionization cones. ESO 137-G034 has a very similar 3–7 keV count rate (0.01 counts s^{-1}) to ESO 428-G014 and NGC 7212, although the exposure time is only ∼1/3, with a total of 441 counts in the 3–7 keV band. The physical extent of the 3–7 keV hard X-ray emission measured along the ionization cone direction is ∼1.0 kpc in radius, comparable to that of ESO 428-G014, with a hint of further extended emission in the N–S direction. For NGC 3281, the 3–7 keV count rate (0.04 counts s^{-1}) is a factor of ∼4 higher than those of ESO 428-G014, NGC 7212, and ESO 137-G034 and is the highest among the entire sample, but the hard extended fraction is the lowest among the four, i.e., more concentrated in the nuclear region. Among the seven CT AGN, only ESO 137-G014 shows extended 6–7 keV (Fe Kα) emission extending >0.65 kpc in radius. Deeper Chandra data are required to consolidate this extended component and reveal the hinted full structure.

Our CT AGN cover a 3–7 keV source count rate range of 0.004–0.04 counts s^{-1}, and we do not observe any correlation between the count rate (or source flux) and the excess counts or extended fraction, although the extended fraction has a strong linear correlation with the excess counts as expected. There appears to be a count rate threshold at ∼0.01 counts s^{-1} combined with a total excess fraction threshold at ∼20% (or an extended fraction threshold at ∼7%) above which a prominent extended hard X-ray morphology is revealed and the excess emission is well detected above the PSF. Of course, a large, complete sample of CT AGN is needed to verify this trend.

Given a total of nine CT AGN with systematically measured excess counts and extended excess fractions, we further investigated whether the measured quantities correlate with any physical parameters (e.g., AGN bolometric luminosity, $N_{\rm H}$), which may give clues to the origin of the extended hard X-ray emission. Figure 10 shows the total excess fraction as a function of $\log N_{\rm H}$. We obtained the $N_{\rm H}$ values from the literature that were mostly constrained though broadband X-ray spectral fitting with a torus model (Ricci et al. 2015, 2017; Baloković 2017; Georgantopoulos & Akylas 2019; Marchesi et al. 2019). These $N_{\rm H}$ values are consistent with our ongoing, preliminary analysis based on NuSTAR spectra. There appears to be a general trend of increasing total excess fraction with $\log N_{\rm H}$. The Pearson correlation coefficient of this sample is 0.43, which suggests a moderate correlation. The correlation

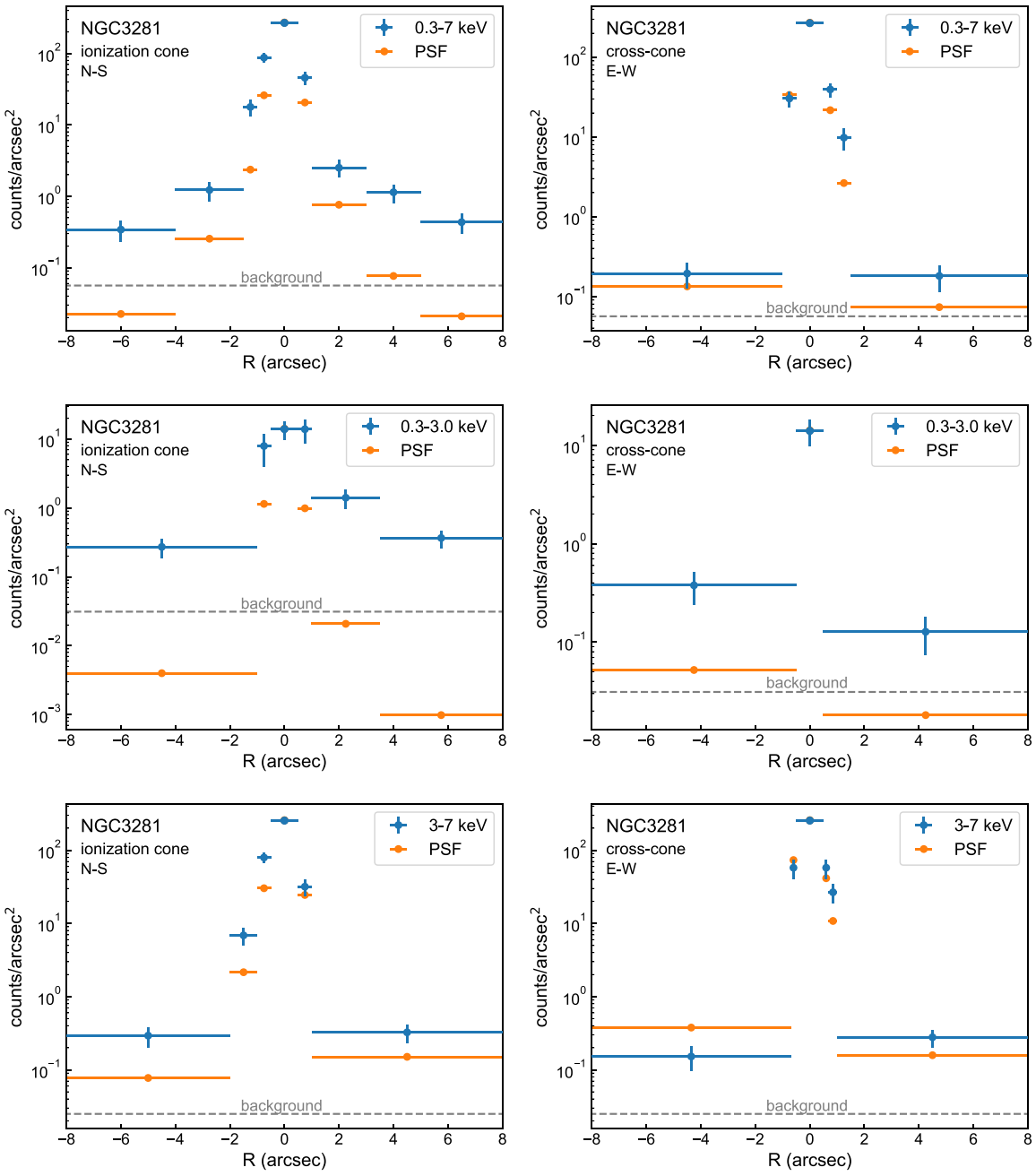

Figure 8. Radial profiles of NGC 3281 in the ionization and cross-cones for the full band, soft band, and hard band. The background has been subtracted off from the radial profiles, the level of which is indicated as the gray dashed horizontal line. The PSF is normalized to the counts in the central 0.″5-radius bin.

seems to be strengthened by a larger sample (M. J. Jones et al. 2020, in preparation). This may imply a connection between the amounts of nuclear obscuration and dense molecular clouds in the host galaxy disk, which supply the materials needed to scatter the X-ray photons and produce the extended component as suggested in ESO 428-G014 (Fabbiano et al. 2017, 2018a, 2018b). This trend also suggests that some of the obscuration may be coming from farther out in the galaxy (not just the torus). Given the current small sample size and the difficulty in constraining $N_{\rm H}$ accurately in this regime, we would need a larger sample with well-constrained $N_{\rm H}$ to verify this trend. No trend is found in other parameter pairs yet.

5.2. Implications on Torus Modeling and AGN Feedback

As to the question of whether the extended hard X-ray emission is ubiquitous in CT AGN, although not all the sources in our sample have extended hard X-ray emission reaching kiloparsec scales ($\geqslant$1 kpc in radius), most of them (five out of seven) do show extended hard X-ray emission above the PSF out to at least $\sim$360 pc in radius, which is beyond the dusty torus in the AGN unified model (e.g., Urry & Padovani 1995; Ramos Almeida & Ricci 2017). We consider the outer edge of the torus to be the radius at which the central BH gravity ceases to dominate over the host galaxy potential, usually corresponding to dust temperature at about 150 K. Using a simple formula (Equation (5)) in Barvainis

Table 4
NGC 3281: The Excess Counts over the Chandra PSF, Extended Fractions, and Total Excess Fractions in the N–S Ionization and E–W Cross-cones

Energy (keV)	N–S Ionization Cone Excess Counts 1.″5–8″	N–S Ionization Cone Excess Counts ⩽1.″5	N–S Ionization Cone Extended Fraction 1.″5–8″	N–S Ionization Cone Total Excess Fraction
0.3–3.0	31.2 ± 5.8 (5.3σ)	13.7 ± 3.9 (3.5σ)	41.7% ± 9.3%[a], 62.0% ± 14.7%[b]	60.0% ± 11.9%[a], 89.2% ± 19.0%[b]
3.0–7.0	16.4 ± 5.2 (3.2σ)	37.5 ± 8.4 (4.5σ)	4.6% ± 1.5%, 9.7% ± 3.2%	15.2% ± 2.9%, 32.0% ± 6.4%
0.3–7.0	50.1 ± 7.8 (6.4σ)	57.7 ± 9.3 (6.2σ)	11.6% ± 1.9%, 22.8% ± 3.9%	25.0% ± 3.1%, 49.2% ± 6.5%
Energy (keV)	E–W cross-cone excess counts 1.″5–8″	E–W cross-cone excess counts ⩽1.″5	E–W cross-cone extended fraction 1.″5–8″	E–W cross-cone total excess fraction
0.3–3.0	10.3 ± 3.8 (2.7σ)	5.0 ± 2.6 (1.9σ)	13.8% ± 5.3%[c], 42.1% ± 18.0%[d]	20.4% ± 6.7%[c], 62.4% ± 23.3%[d]
3.0–7.0	<9.6	<21.8	<2.7%, <5.1%	<6.7%, <12.7%
0.3–7.0	9.7 ± 5.0 (2.0σ)	16.0 ± 7.7 (2.1σ)	2.3% ± 1.2%, 4.6% ± 2.4%	6.0% ± 2.2%, 12.1% ± 4.4%

Notes. We place a 3σ upper limit if there are no excess counts above the PSF (i.e., <1σ).
[a] The first fraction is the excess counts in the extended region of the N–S ionization bicone relative to the total counts within the 8″-radius circle at the given energy band.
[b] The second fraction is the excess counts in the extended region of the N–S ionization bicone relative to the total counts in the bicone itself at the given energy band.
[c] The first fraction is the excess counts in the extended region of the E–W cross-cones relative to the total counts within the 8″-radius circle at the given energy band.
[d] The second fraction is the excess counts in the extended region of the E–W cross-cones relative to the total counts in the cross-cones at the given energy band.

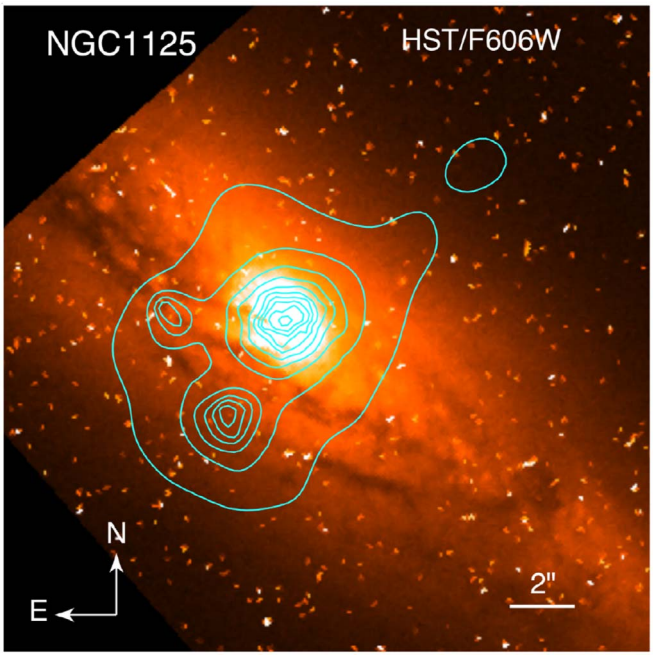

Figure 9. 20″ × 20″ HST/F606W image of NGC 1125 (Malkan et al. 1998), an SB0/a galaxy hosting a Seyfert 2 nucleus. The Chandra 0.3–7.0 keV X-ray contours are overlaid in cyan, extending perpendicular to the major axis of the host galaxy out to 8″ in radius. The nearby two X-ray-detected sources have no optical counterparts.

(1987), we estimated that the outer torus radii for the seven CT AGN are in the range of ∼33–113 pc. Detecting hard X-ray emission beyond the traditional dusty torus in the standard AGN unified model implies that we need to test and improve torus modeling and update our knowledge of SMBH–host galaxy interactions.

The seven CT AGN in our sample and ESO 428-G014 all have high-quality, broadband NuSTAR spectra covering 3–79 keV, which we will present in a future publication. In principle, aspects of the obscuring torus geometry, e.g., its scale height, opening angle, inclination angle, and torus covering factor in clumpy torus models (Elitzur 2008; Nenkova et al. 2008), can all be extracted from observed broadband X-ray spectra of AGN (e.g., with NuSTAR) with the help of parameterized spectral models (e.g., Murphy & Yaqoob 2009; Baloković et al. 2018; Tanimoto et al. 2019). However, the existence of reprocessed emission on >100 pc scales (i.e., outside of the compact torus) is currently not accounted for by any published models. This newly discovered component, if ignored, can lead to biased estimates of the torus covering factor and/or its average column density. For example, our preliminary analysis of spatially resolved data for ESO 428-G014 suggests that its torus covering factor may be significantly lower (by almost a factor of two depending on the modeling details) compared to a spatially unresolved spectral analysis (M. B. Baloković et al. 2020, in preparation).

It is possible that the opening angle and the internal covering factor within the torus can be derived from the extended X-ray and other measures. This may reduce the degrees of freedom in torus models, as they usually contain many free parameters (e.g., Murphy & Yaqoob 2009; Baloković et al. 2018; Tanimoto et al. 2019), and therefore reduce the uncertainties in the remaining torus model parameters. The Chandra detections of the extended hard X-ray emission in ESO 428-G014, ESO 137-G034, and NGC 3281 can serve as test beds for this purpose.

The extended hard X-ray emission appears not only in the direction of ionization cones but also in the cross-cone regions, as clearly shown in ESO 428-G014 (Fabbiano et al. 2017, 2018a) and NGC 7212 (Jones et al. 2020). Rather than a completely obscuring torus in the standard AGN unified model, the appearance of extended hard X-ray emission supports the increasingly popular scenario of a clumpy structure of the torus (e.g., Nenkova et al. 2002, 2008; Elitzur 2012), which allows for the transmission of radiation on kiloparsec scales. The interactions of the photons escaping the nuclear region with the ISM clouds in the host galaxy would give rise to the extended diffuse emission in both the ionization cone and cross-cone directions (Fabbiano et al. 2018a, 2018b). The X-ray emission of these sources is also accompanied by the presence of radio jets (Fabbiano et al. 2018b; Jones et al. 2020). The jet–cold disk ISM interactions may form a very hot cocoon enclosing

Table 5
Literature Comparison Sample of Extended Hard X-Ray Emission: The Excess Counts over the Chandra PSF, Extended Fractions, and Total Excess Fractions

Source Name	z	3.0–7.0 keV Excess Counts $1\farcs5$–$8''$	3.0–7.0 keV Excess Counts $\leqslant 1\farcs5$	3.0–7.0 keV Total Excess Counts	3.0–7.0 keV Extended Fraction $1\farcs5$–$8''$	3.0–7.0 keV Total Excess Fraction
ESO 428-G014	0.00566	318.4 ± 19.9 (16.0σ)	144.6 ± 24.3 (6.0σ)	462.9 ± 31.4 (14.8σ)	$20.8\% \pm 1.4\%$	$30.2\% \pm 2.2\%$
NGC 7212	0.0266	226.0 ± 15.0 (15.1σ)	323.5 ± 18.0 (18.0σ)	549.5 ± 23.4 (23.5σ)	$14.7\% \pm 1.0\%$	$35.7\% \pm 1.8\%$
		6.0–7.0 keV excess counts $1\farcs5$–$8''$	6.0–7.0 keV excess counts $\leqslant 1\farcs5$	6.0–7.0 keV total excess counts	6.0–7.0 keV extended fraction $1\farcs5$–$8''$	6.0–7.0 keV total excess fraction
ESO 428-G014		52.4 ± 9.1 (5.7σ)	20.5 ± 13.3 (1.5σ)	72.8 ± 16.2 (4.5σ)	$11.8\% \pm 2.1\%$	$16.4\% \pm 3.7\%$
NGC 7212		27.3 ± 5.2 (5.3σ)	68.4 ± 8.3 (8.2σ)	95.7 ± 9.8 (9.8σ)	$7.3\% \pm 1.4\%$	$25.5\% \pm 2.9\%$

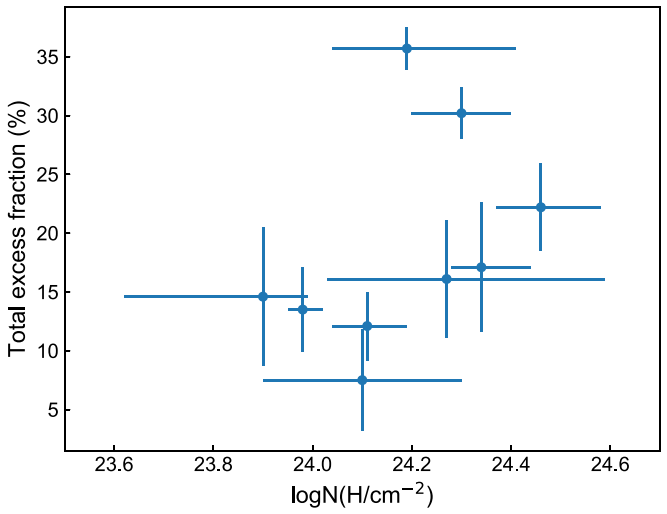

Figure 10. Total excess fraction at 3–7 keV vs. log $N_{\rm H}$ of the nine CT AGN. There appears to be a general trend of increasing total excess fraction with log $N_{\rm H}$.

the interaction region, which could contribute to the X-ray emission seen in the cross-cone region. This hot cocoon has been predicted by relativistic hydrodynamical simulations (e.g., Mukherjee et al. 2018) and provides an alternative explanation to the X-ray emission perpendicular to the ionization cone direction.

The extended 3–6 keV continuum and Fe Kα emission, as in ESO 428-G014, are explained as being due to electron scattering off dense ISM clouds in the host galaxy (Fabbiano et al. 2017, 2018a). ALMA CO (2−1) and SINFONI H_2 2.12 μm observations reveal that the hard X-ray emission overlaps with warm H_2, where CO (2−1) shows a cavity (Feruglio et al. 2020). A similar case was reported in NGC 2110 by Fabbiano et al. (2019) and Rosario et al. (2019). This suggests that the scattering material giving rise to the extended hard X-ray emission is warm molecular gas, and CO may be excited to higher-J levels by AGN hard X-ray irradiation and/or shocks. The spatial anticorrelation of hard X-ray emission and dense molecular clouds is also reported in the Circinus galaxy (Kawamuro et al. 2019). It is likely that the molecular gas is efficiently dissociated by AGN X-ray irradiation, leaving an X-ray-dominated region. The X-ray irradiation has the potential to consequently suppress star formation. Such observations of molecular gas in the circumnuclear regions of ESO 137-G034 and NGC 3281 will help uncover the origin and mechanism behind the extended hard X-ray emission detected by Chandra.

6. Summary and Conclusions

We performed a Chandra spatial analysis of a sample of seven uniformly selected nearby CT AGN to investigate the extended hard X-ray component, and we measure the excess counts, extended fractions, and physical scales. Five of them show extended emission in the 3–7 keV band detected at $>3\sigma$, with total excess fractions ranging from $\sim$12% to 22%. Among the seven CT AGN, ESO 137-G034 and NGC 3281 are the two sources that display biconical ionization structures, with the extended hard X-ray emission reaching kiloparsec scales. ESO 137-G034 exhibits the most prominent extended hard X-ray emission, with 22% of the 3–7 keV emission detected in the extended component. The spatial extent reaches $\sim$1.9 kpc in diameter with a tendency to extend farther. The extended hard X-ray emission is also well detected in NGC 3281 in the ionization biconical region with a total excess fraction of $\sim$14% and a spatial extent of $\sim$3.5 kpc in diameter. Three additional sources show extended hard X-ray emission above the PSF out to $\sim$360 pc in radius at least. The extended emission in the 0.3–3.0 keV soft band is well detected in most of the sources, except ESO 005-G004 and J0025+6821.

We compared the properties of the seven CT AGN with two other CT AGN with well-detected kiloparsec-scale extended hard X-ray emission, ESO 428-G014 and NGC 7212. Based on these nine CT AGN, we find a trend that the detection of a prominent extended hard component requires a 3–7 keV count rate threshold at $\sim$0.01 counts s^{-1} combined with a total extended excess fraction of $>\sim$20%. Since this is a relatively shallow pilot survey, a complete sample with deep Chandra data will improve the statistics and reveal full X-ray ionization structures, e.g., in ESO 137-G034, where a Z-shaped morphology has been revealed in the optical emission-line maps.

We discussed the need to incorporate the extended hard X-ray component in torus modeling in order both to remove emission not associated with the torus that may bias the results and to provide input parameters to the torus model, reducing the number of degrees of freedom. More torus modeling work is under way to test the effects induced by including this new component (Baloković et al. 2020, in preparation). The Chandra detections of the extended hard X-ray emission in, e.g., ESO 428-G014 and ESO 137-G034, can serve as test beds for improving torus modeling.

The extended hard X-ray component provides a new window to investigating how the central SMBH interacts with and impacts the host galaxy at large scales. Future combined, high-resolution observations and analyses of the optical emission lines, radio jets, molecular gas, and X-ray emission will unveil the interaction/feedback mechanisms and improve our understanding of AGN–host galaxy connection.

We thank Raffaella Morganti for providing the ATCA radio data for our analysis. This work makes use of data from the Chandra data archive and the NASA-IPAC Extragalactic Database (NED). The analysis makes use of CIAO and Sherpa, developed by the Chandra X-ray Center; SAOImage ds9; XSPEC, developed by HEASARC at NASA-GSFC; and the Astrophysics Data System (ADS). This work also uses observations made with the NASA/ESA Hubble Space Telescope, obtained from the data archive at the Space Telescope Science Institute. This work was supported by the Chandra Guest Observer program, grant No. GO9-20088X (PI: Elvis). M.B. acknowledges support from the black hole Initiative at Harvard University, which is funded in part by the Gordon and Betty Moore Foundation (grant GBMF8273) and in part by the John Templeton Foundation.

Appendix
Additional Images and Radial Profiles

For NGC 424, NGC 1125, NGC 4500, ESO 005-G004, and J0025+6821, the Chandra images do not show obvious ionization cones and cross-cones, so we generated the radial profiles over all azimuthal angles. The Chandra soft-band (0.3–3 keV) and hard-band (3–7 keV) images and their adaptively smoothed versions are shown in Figures A1, A3, A5, A7, and A9. The corresponding radial profiles in the

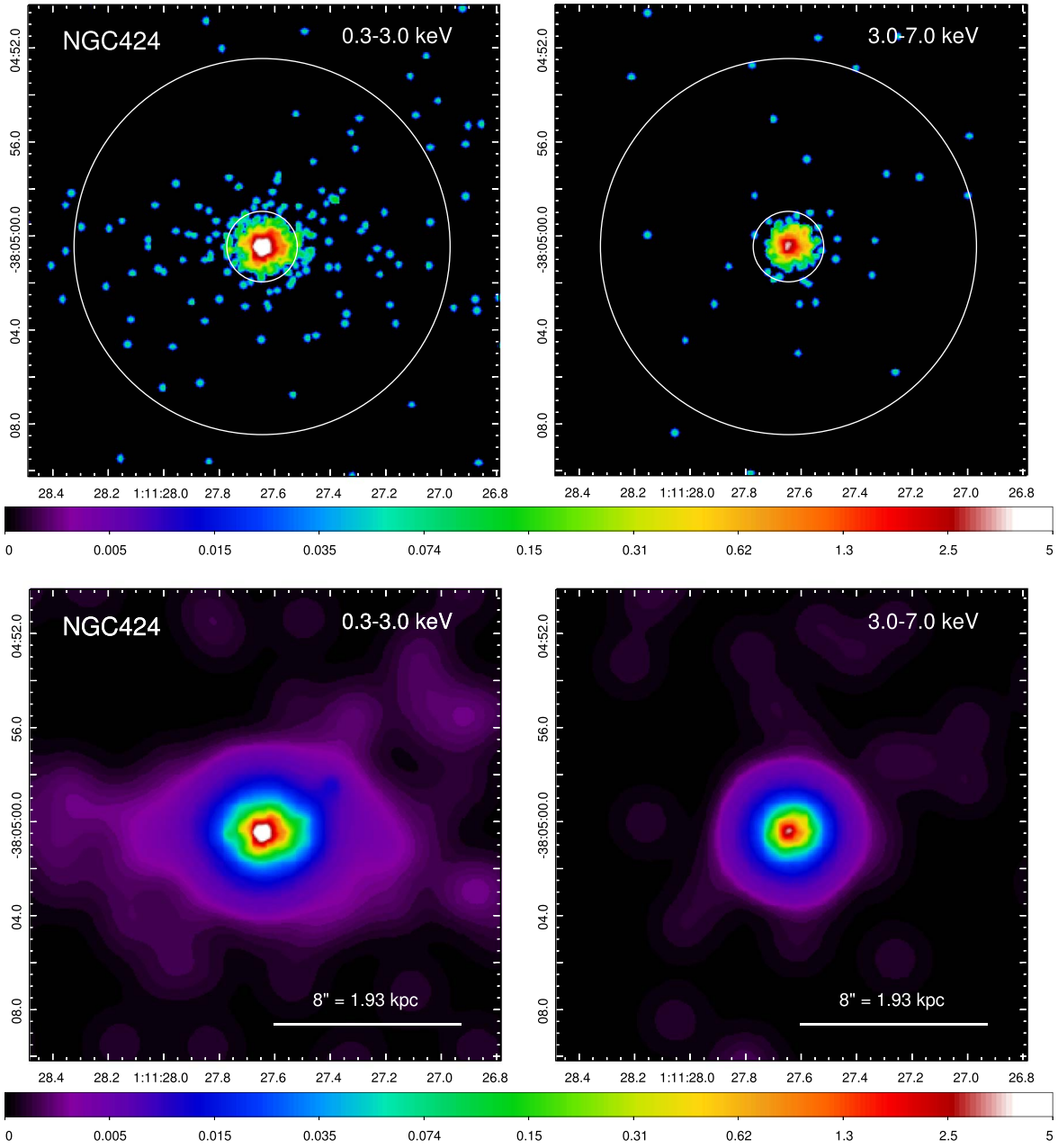

Figure A1. Top: 20″ × 20″ merged Chandra ACIS-S 0.3–3.0 keV (left) and 3.0–7.0 keV (right) band images of NGC 424 at 1/8 subpixel binning. The inner 1.″5-radius circle and the outer 8″-radius circle define the region in between for extracting excess counts in the extended emission. Bottom: adaptively smoothed images (*dmimgadapt*; 0.5–15 pixel scales, 5 counts under kernel, 30 iterations) on 1/8 binned pixel. All the images are displayed in logarithmic scale, with colors corresponding to the counts per image pixel.

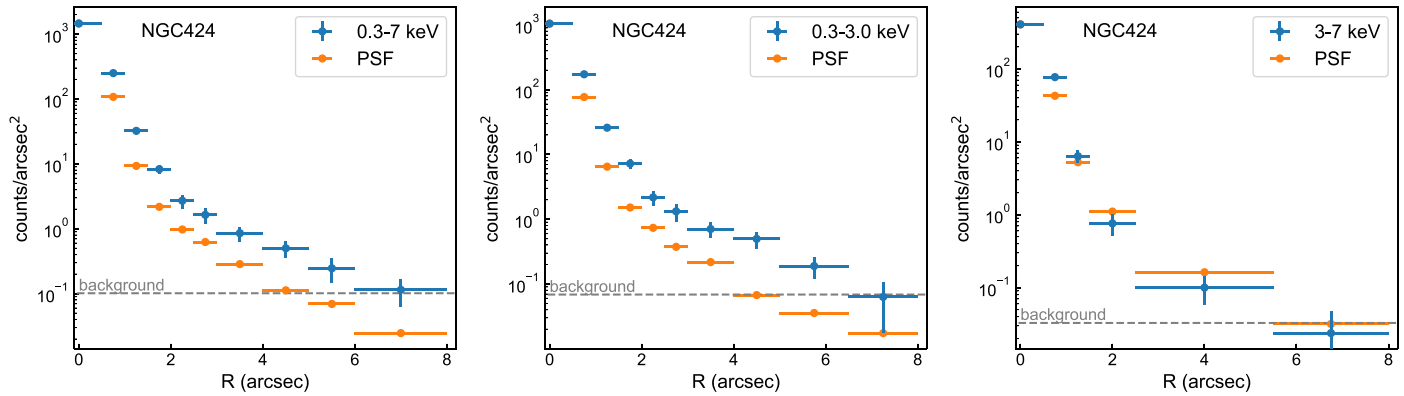

Figure A2. Radial profiles of NGC 424 for the full band, soft band, and hard band. The background has been subtracted off from the radial profiles, the level of which is indicated as the gray dashed horizontal line. The PSF is normalized to the counts in the central $0\farcs5$-radius bin.

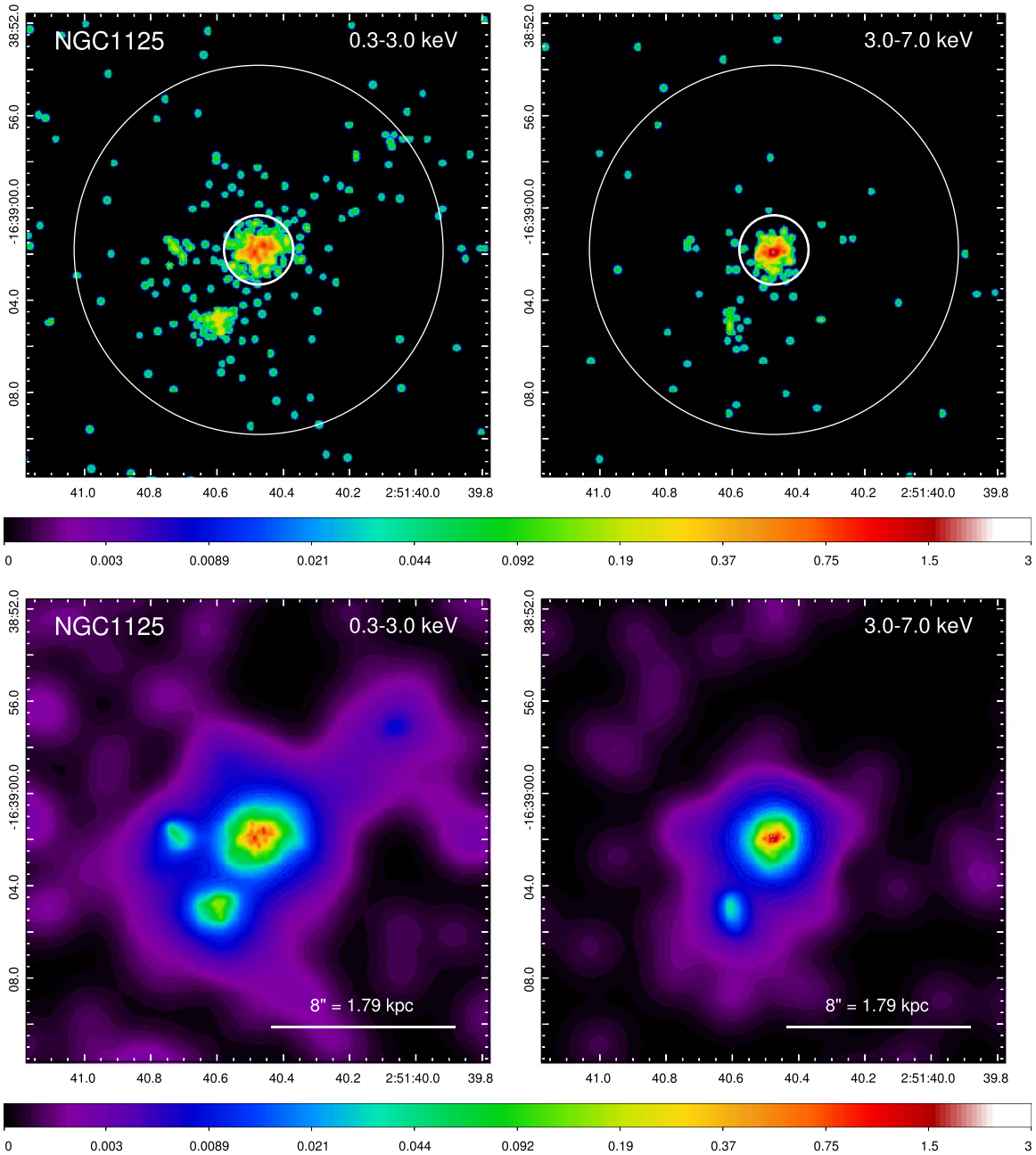

Figure A3. Top: $20'' \times 20''$ Chandra ACIS-S 0.3–3.0 keV (left) and 3.0–7.0 keV (right) band images of NGC 1125 at $1/8$ subpixel binning. The inner $1\overset{''}{.}5$-radius circle and the outer $8''$-radius circle define the region in between for extracting excess counts in the extended emission. Bottom: adaptively smoothed images (*dmimgadapt*; 0.5–15 pixel scales, 5 counts under kernel, 30 iterations) on $1/8$ binned pixel. All the images are displayed in logarithmic scale, with colors corresponding to the counts per image pixel.

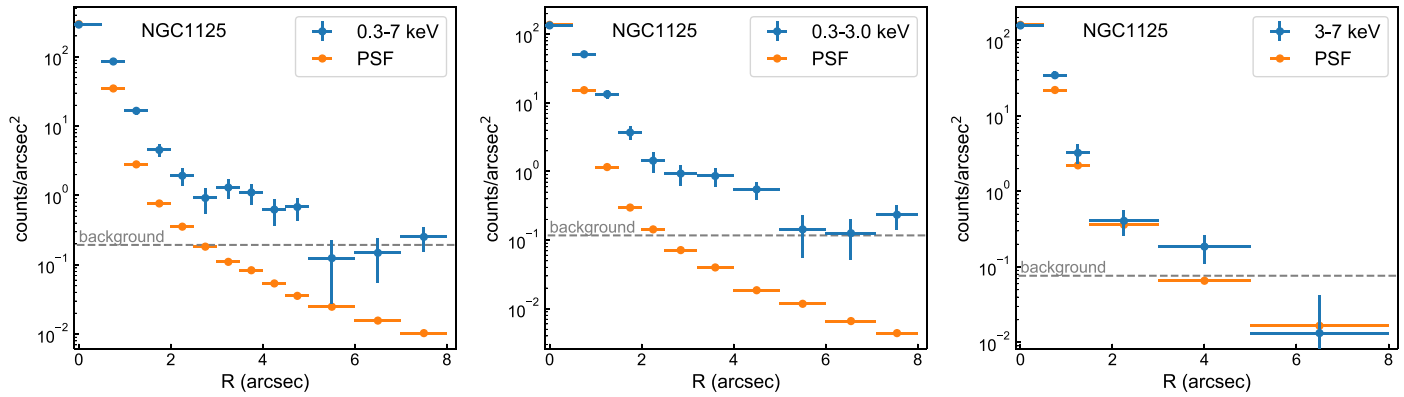

Figure A4. Radial profiles of NGC 1125 for the full band, soft band, and hard band. The background has been subtracted off from the radial profiles, the level of which is indicated as the gray dashed horizontal line. The PSF is normalized to the counts in the central $0\farcs5$-radius bin. The two X-ray sources detected off-center were removed before generating the radial profiles.

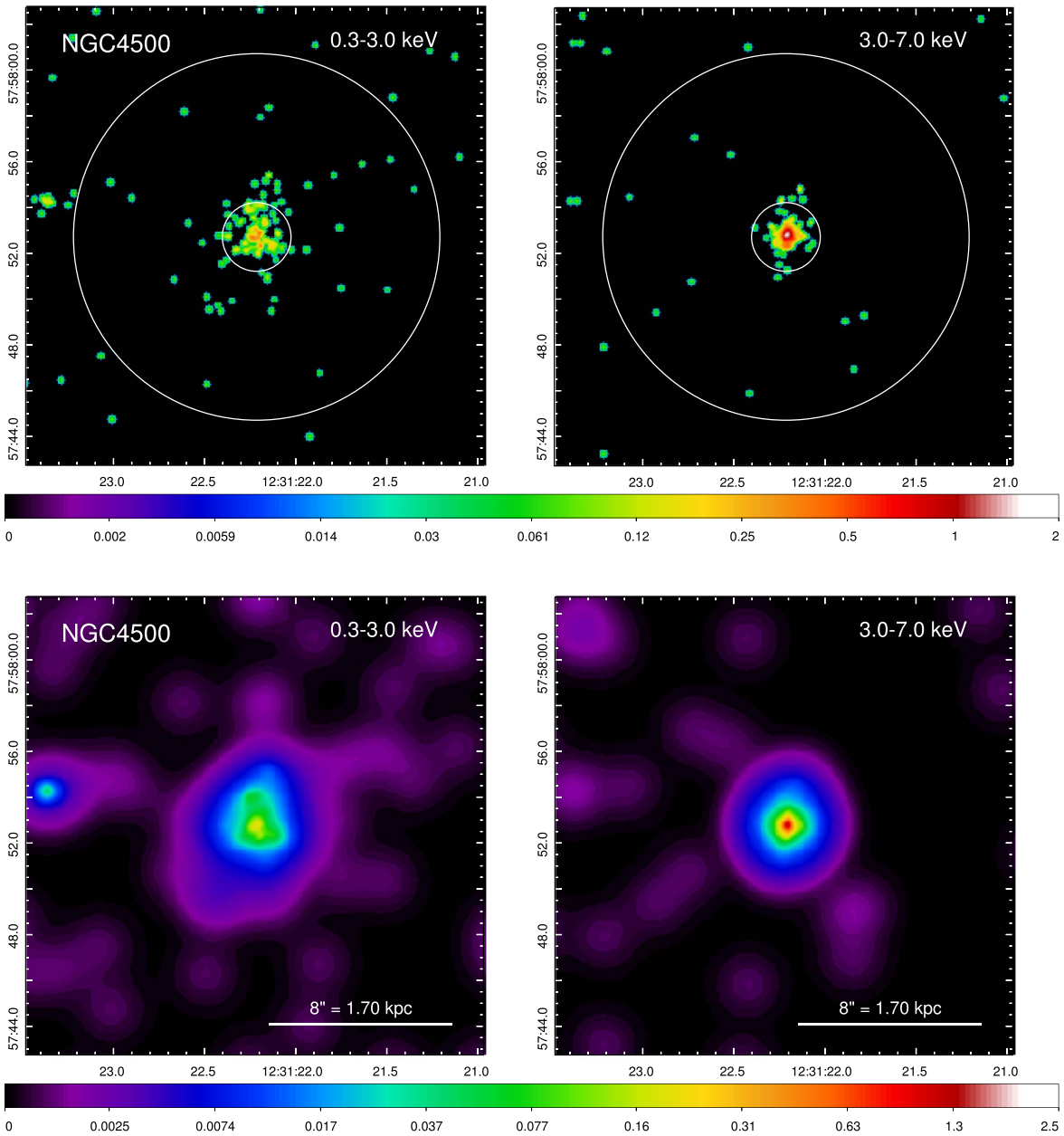

Figure A5. Top: $20'' \times 20''$ Chandra ACIS-S 0.3–3.0 keV (left) and 3.0–7.0 keV (right) band images of NGC 4500 at $1/8$ subpixel binning. The inner $1\overset{''}{.}5$-radius circle and the outer $8''$-radius circle define the region in between for extracting excess counts in the extended emission. Bottom: adaptively smoothed images (*dmimgadapt*; 0.5–15 pixel scales, 5 counts under kernel, 30 iterations) on $1/8$ binned pixel. All the images are displayed in logarithmic scale, with colors corresponding to the counts per image pixel.

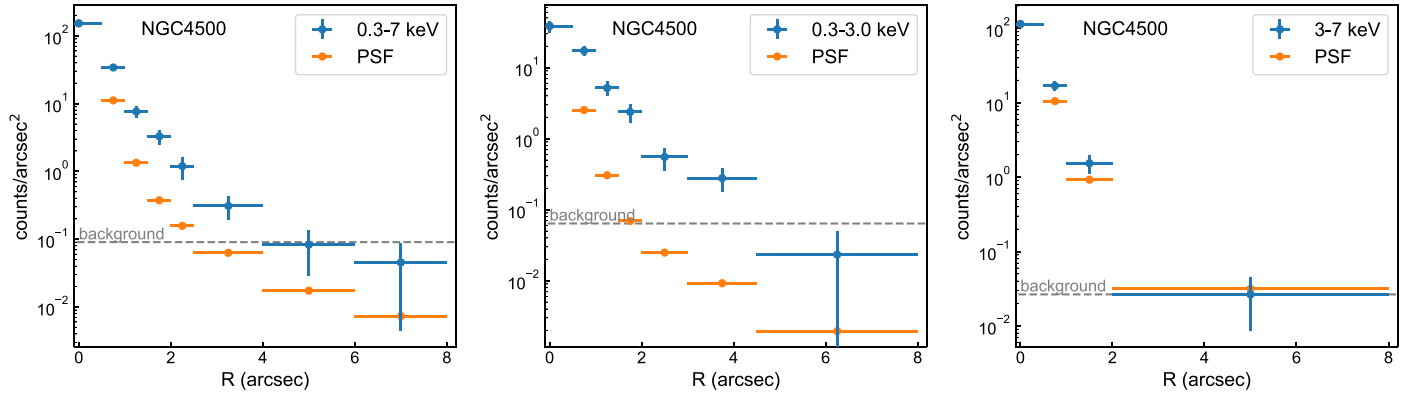

Figure A6. Radial profiles of NGC 4500 for the full band, soft band, and hard band. The background has been subtracted off from the radial profiles, the level of which is indicated as the gray dashed horizontal line. The PSF is normalized to the counts in the central $0\farcs5$-radius bin.

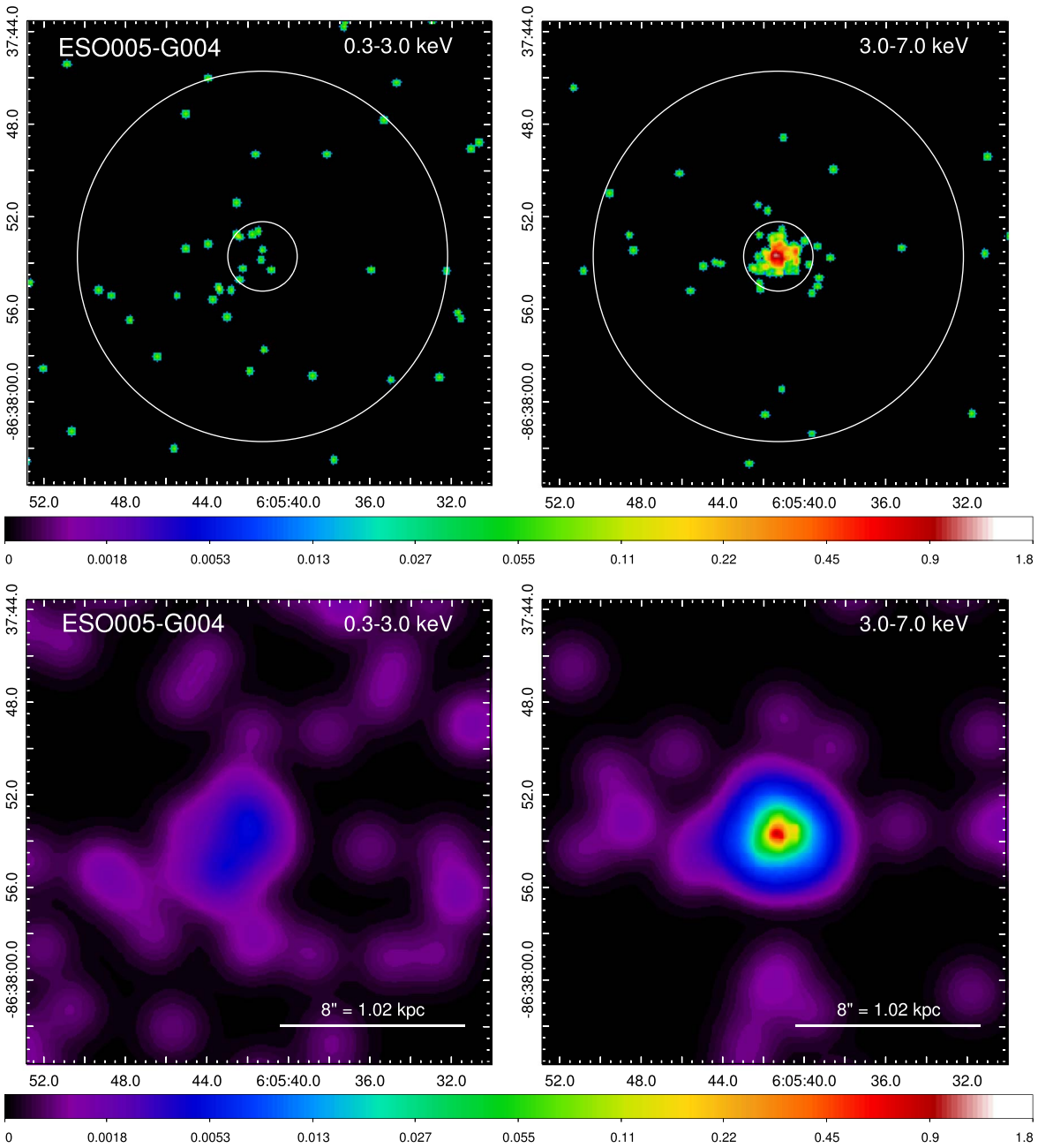

Figure A7. Top: $20'' \times 20''$ Chandra ACIS-S 0.3–3.0 keV (left) and 3.0–7.0 keV (right) band images of ESO 005-G004 at $1/8$ subpixel binning. The inner $1\farcs5$-radius circle and the outer $8''$-radius circle define the region in between for extracting excess counts in the extended emission. Bottom: adaptively smoothed images (*dmimgadapt*; 0.5–15 pixel scales, 5 counts under kernel, 30 iterations) on $1/8$ binned pixel. All the images are displayed in logarithmic scale, with colors corresponding to the counts per image pixel.

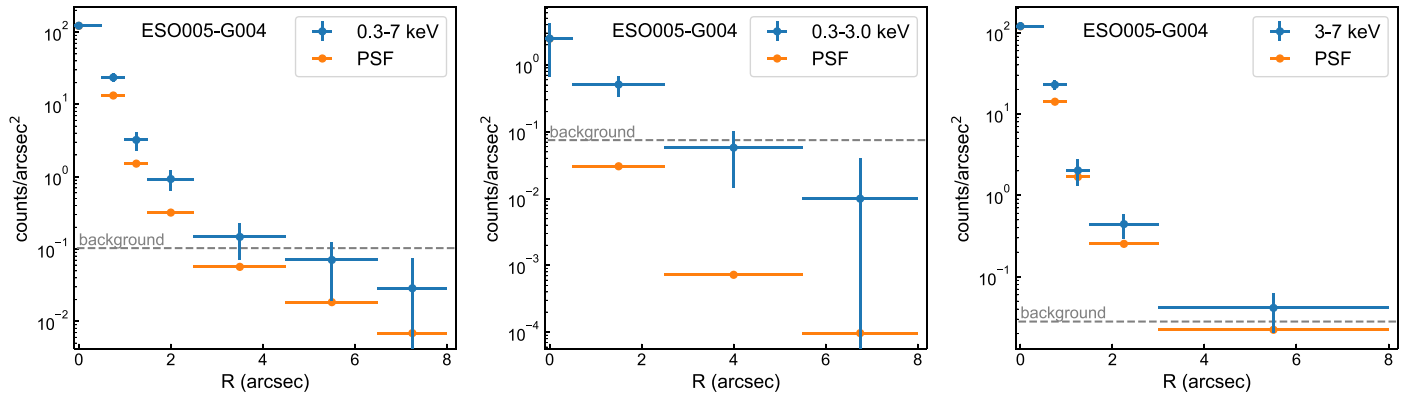

Figure A8. Radial profiles of ESO 005-G004 for the full band, soft band, and hard band. The background has been subtracted off from the radial profiles, the level of which is indicated as the gray dashed horizontal line. The PSF is normalized to the counts in the central $0\farcs5$-radius bin.

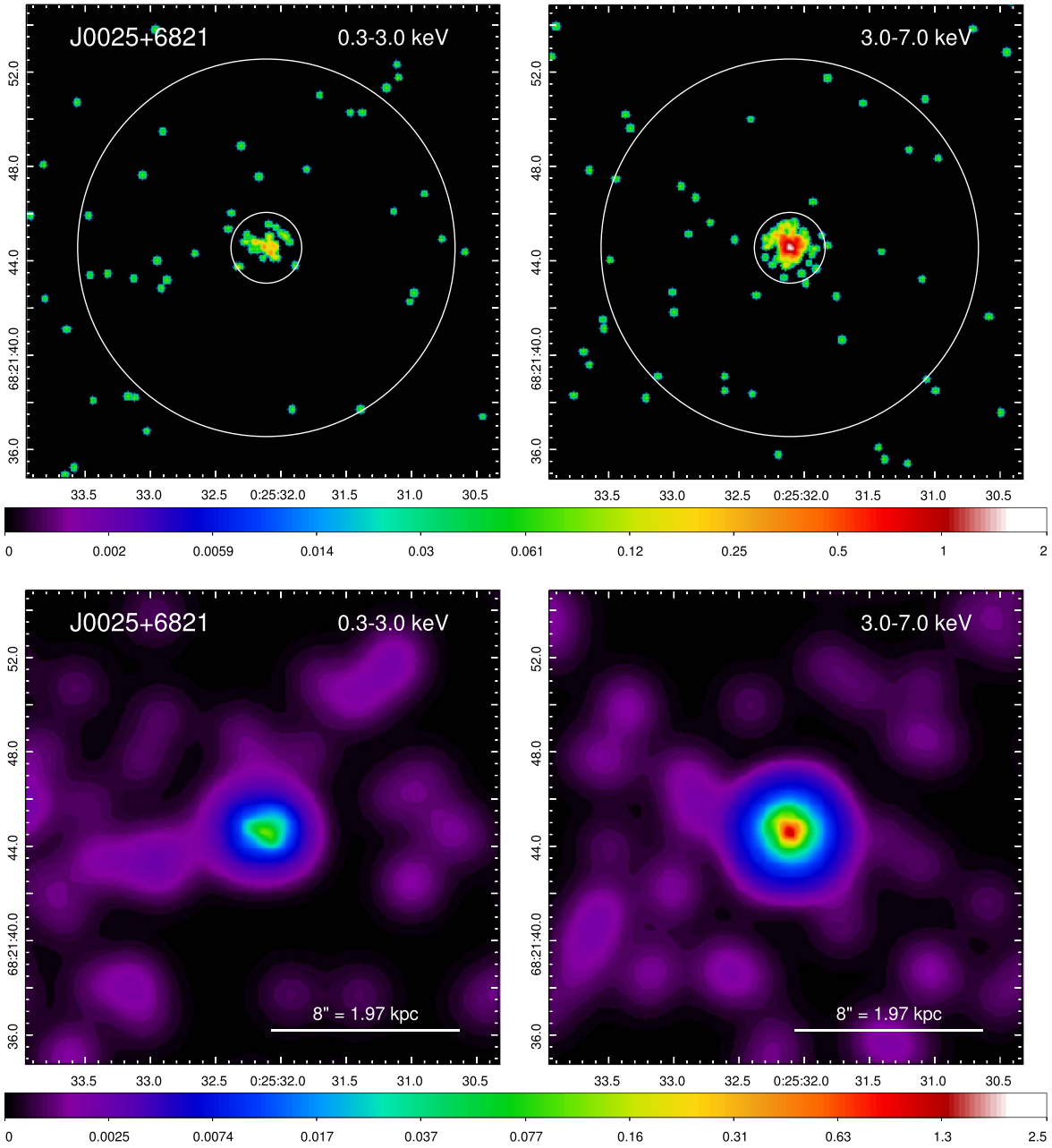

Figure A9. Top: 20″ × 20″ merged Chandra ACIS-S 0.3–3.0 keV (left) and 3.0–7.0 keV (right) band images of J0025+6821 at 1/8 subpixel binning. The inner 1.″5-radius circle and the outer 8″-radius circle define the region in between for extracting excess counts in the extended emission. Bottom: adaptively smoothed images (*dmimgadapt*; 0.5–15 pixel scales, 5 counts under kernel, 30 iterations) on 1/8 binned pixel. All the images are displayed in logarithmic scale, with colors corresponding to the counts per image pixel.

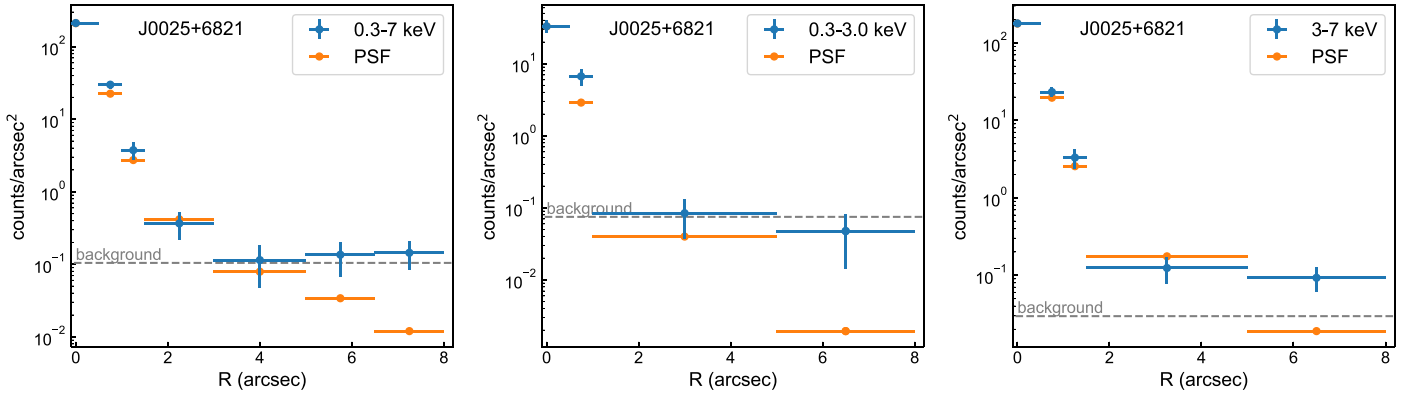

Figure A10. Radial profiles of J0025+6821 for the full band, soft band, and hard band. The background has been subtracted off from the radial profiles, the level of which is indicated as the gray dashed horizontal line. The PSF is normalized to the counts in the central 0.″5-radius bin.

0.3–3 keV, 3–7 keV, and 0.3–7 keV bands are shown in Figures A2, A4, A6, A8, and A10, respectively.

ORCID iDs

Jingzhe Ma https://orcid.org/0000-0003-4178-0800
Martin Elvis https://orcid.org/0000-0001-5060-1398
G. Fabbiano https://orcid.org/0000-0002-3554-3318
Mislav Baloković https://orcid.org/0000-0003-0476-6647
W. Peter Maksym https://orcid.org/0000-0002-2203-7889
Mackenzie L. Jones https://orcid.org/0000-0003-4814-8752
Guido Risaliti https://orcid.org/0000-0002-3556-977X

References

Antonucci, R. 1993, ARA&A, 31, 473
Arévalo, P., Bauer, F. E., Puccetti, S., et al. 2014, ApJ, 791, 81
Baloković, M. 2017, PhD thesis, CalTech
Baloković, M., Brightman, M., Harrison, F. A., et al. 2018, ApJ, 854, 42
Baloković, M., Comastri, A., Harrison, F. A., et al. 2014, ApJ, 794, 111
Balzano, V. A. 1983, ApJ, 268, 602
Barvainis, R. 1987, ApJ, 320, 537
Bauer, F. E., Arévalo, P., Walton, D. J., et al. 2015, ApJ, 812, 116
Bianchi, S., Guainazzi, M., & Chiaberge, M. 2006, A&A, 448, 499
Chou, R. C. Y., Peck, A. B., Lim, J., et al. 2007, ApJ, 670, 116
Elitzur, M. 2008, NewAR, 52, 274
Elitzur, M. 2012, ApJL, 747, L33
Fabbiano, G., Elvis, M., Paggi, A., et al. 2017, ApJL, 842, L4
Fabbiano, G., Paggi, A., Karovska, M., et al. 2018a, ApJ, 855, 131
Fabbiano, G., Paggi, A., Karovska, M., et al. 2018b, ApJ, 865, 83
Fabbiano, G., Siemiginowska, A., Paggi, A., et al. 2019, ApJ, 870, 69
Farrah, D., Baloković, M., Stern, D., et al. 2016, ApJ, 831, 76
Ferruit, P., Wilson, A. S., & Mulchaey, J. 2000, ApJS, 128, 139
Feruglio, C., Fabbiano, G., Bischetti, M., et al. 2020, ApJ, 890, 29
Fruscione, A., McDowell, J. C., Allen, G. E., et al. 2006, Proc. SPIE, 6270, 62701V
Georgantopoulos, I., & Akylas, A. 2019, A&A, 621, A28
Jones, M. L., Fabbiano, G., Elvis, M., et al. 2020, ApJ, 891, 133
Kawamuro, T., Izumi, T., & Imanishi, M. 2019, PASJ, 71, 68
Koss, M., Trakhtenbrot, B., Ricci, C., et al. 2017, ApJ, 850, 74
Koss, M. J., Romero-Cañizales, C., Baronchelli, L., et al. 2015, ApJ, 807, 149
Levenson, N. A., Heckman, T. M., Krolik, J. H., et al. 2006, ApJ, 648, 111
Maksym, W. P., Fabbiano, G., Elvis, M., et al. 2017, ApJ, 844, 69
Maksym, W. P., Fabbiano, G., Elvis, M., et al. 2019, ApJ, 872, 94
Malkan, M. A., Gorjian, V., & Tam, R. 1998, ApJS, 117, 25
Marchesi, S., Ajello, M., Zhao, X., et al. 2019, ApJ, 872, 8
Marinucci, A., Bianchi, S., Fabbiano, G., et al. 2017, MNRAS, 470, 4039
Marinucci, A., Risaliti, G., Wang, J., et al. 2012, MNRAS, 423, L6
Morganti, R., Tsvetanov, Z. I., Gallimore, J., et al. 1999, A&AS, 137, 457
Mukherjee, D., Wagner, A. Y., Bicknell, G. V., et al. 2018, MNRAS, 476, 80
Murphy, K. D., & Yaqoob, T. 2009, MNRAS, 397, 1549
Nenkova, M., Ivezić, Ž, & Elitzur, M. 2002, ApJL, 570, L9
Nenkova, M., Sirocky, M. M., Nikutta, R., et al. 2008, ApJ, 685, 160
Netzer, H. 2015, ARA&A, 53, 365
Paggi, A., Wang, J., Fabbiano, G., et al. 2012, ApJ, 756, 39
Paltani, S., & Ricci, C. 2017, A&A, 607, A31
Ramos Almeida, C., & Ricci, C. 2017, NatAs, 1, 679
Ricci, C., Trakhtenbrot, B., Koss, M. J., et al. 2017, ApJS, 233, 17
Ricci, C., Ueda, Y., Koss, M. J., et al. 2015, ApJL, 815, L13
Rosario, D. J., Togi, A., Burtscher, L., et al. 2019, ApJL, 875, L8
Schmitt, H. R., Donley, J. L., Antonucci, R. R. J., et al. 2003a, ApJS, 148, 327
Schmitt, H. R., Donley, J. L., Antonucci, R. R. J., et al. 2003b, ApJ, 597, 768
Storchi-Bergmann, T., Wilson, A. S., & Baldwin, J. A. 1992, ApJ, 396, 45
Tanimoto, A., Ueda, Y., Odaka, H., et al. 2019, ApJ, 877, 95
Urry, C. M., & Padovani, P. 1995, PASP, 107, 803
Vasylenko, A. A., Fedorova, E., & Zhdanov, V. I. 2013, AASP, 3, 120
Véron-Cetty, M.-P., & Véron, P. 2006, A&A, 455, 773
Wang, J., Fabbiano, G., Elvis, M., et al. 2011a, ApJ, 736, 62
Wang, J., Fabbiano, G., Elvis, M., et al. 2011b, ApJ, 742, 23
Wang, J., Fabbiano, G., Risaliti, G., et al. 2011c, ApJ, 729, 75